Additively-manufactured Deterministic Porous Structures for Transpiration Cooling

by

Kevin Zhang

A thesis
presented to the University of Waterloo
in fulfillment of the
thesis requirement for the degree of
Master of Applied Science
in
Mechanical and Mechatronics Engineering

Waterloo, Ontario, Canada, 2023

Author's Declaration

I hereby declare that I am the sole author of this thesis. This is a true copy of the thesis, including any required final revisions, as accepted by my examiners.

I understand that my thesis may be made electronically available to the public.

Abstract

Transpiration cooling is increasingly being studied as a method of thermal protection in hypersonic flight, rocket engine liners, and gas turbines. To date, materials for transpiration cooling have been restricted to porous ceramic composites and sintered metal foams. Advances in additive manufacturing have enabled the creation of architected lattices, which have deterministic mesostructures. One such family of lattices are triply-periodic minimal surfaces (TPMS), which are continuous, analytically-defined, repeating 3D geometries. Additively-manufactured metal TPMS structures are already being studied for biomedical applications and it is proposed that they could offer several advantages for transpiration cooling as well: high surface area-to-volume ratio, pore inter-connectivity, and mechanical strength. In this thesis, the fluid flow behaviour through gyroid TPMS lattices is investigated through computational fluid dynamics simulation, using the lattice Boltzmann method (LBM). A comparison is made between ideal geometry and the as-printed geometry of samples fabricated with laser powder bed fusion and characterized using X-ray computed tomography. The results of this analysis are applied to manufacture and simulate two different leading edge structures using functionally graded TPMS in an attempt to produce non-uniform flow permeability in a more practical context. In all cases, permeability of the as-printed parts was lower than for their respective designs, due to the irregular surface morphology. Further complications were introduced by the presence of over- and underprinting. These results highlight the importance of considering performance deviation in actual manufactured parts. The outcomes of this research will assist in developing a methodology for the design optimization via performance simulation of these structures to meet fluid flow requirements for transpiration cooling applications.

Acknowledgements

I would like to thank my advisors, Dr. Jean-Pierre Hickey and Dr. Mihaela Vlasea, for their unending support, knowledge, and patience. This research was made possible by funding support provided by the Federal Economic Development Agency for Southern Ontario (FedDev Ontario grant number 081885) and by support provided by the Multi-Scale Additive Manufacturing Laboratory at the University of Waterloo. In particular, I would like to thank Mr. Jerry Ratthapakdee, who assisted with fabrication of the samples, as well as Mr. Henry Ma, who assisted with the X-ray computed tomography and image processing. The simulations in this thesis were enabled in part by the high-performance computing resources offered through SciNet (https://www.scinethpc.ca/), SHARCNet (https://www.sharcnet.ca/), and the Digital Research Alliance of Canada (https://alliancecan.ca//). I would also like to acknowledge the financial support of the University of Waterloo Engineering Excellence Fellowship.

Table of Contents

List of Figures

List of Tables

Chapter 1

Introduction

1.1 Motivation

Modern aerospace operations are becoming increasingly characterized by extreme temperatures and speeds, far beyond the limits of conventional materials. Such adverse conditions are present in both external aerodynamics (reentry vehicles, hypersonics) and internal aerodynamics (combustion chambers, nozzles, gas turbines, etc.).

The strategies for mitigating heat loads caused by aerothermal heating or combustion are broadly termed "thermal protection systems" (TPS). The first generation of TPS were passive systems, either exotic high temperature materials, or an outer coating of sacrificial (ablative) material. These early approaches can be seen, for example, in the ceramic/composite insulation of the Space Shuttle, and the ablative heat shields of the Apollo command modules. These methods are straightforward to implement, but can be costly and inefficient. Research efforts since then have focused on the development of more reusable and economical TPS. One such promising technology is transpiration cooling.

Transpiration cooling consists of moving a fluid via a pressure gradient through a porous medium into a boundary layer. Coolant passing through the porous material absorbs heat through convective heat transfer. As the coolant exits the material, it forms a layer along the external surface, producing a film cooling effect. The heated coolant is advected

downstream and replaced by new coolant flowing from the porous surface. Transpiration cooling has been shown to provide better performance compared to regenerative cooling and standard film cooling [1].

To date, materials for transpiration cooling applications are mostly restricted to porous composites (particularly ceramic-matrix composites) and sintered metal foams [2]. These can be considered stochastic materials, since only their bulk porosity and structure can be controlled. In contrast, the rise of additive manufacturing (AM) has enabled the realization of design-driven porous architectures: materials with controllable mesostructures that allow for fluid transport. This presents a clear opportunity for use in transpiration cooling. By varying the size and shape of an AM-fabricated porous structure, at global or local scales, the flow behaviour can be influenced in order to meet given performance targets.

One particularly interesting class of architected geometries are triply-periodic minimal surfaces (TPMS). These structures are mathematically-defined isosurfaces and are typically characterized by smooth, winding channels. TPMS structures have the potential to be suitable candidates for transpiration cooling. Their high surface area-to-volume ratio [3] compared to other structures of similar porosity could produce increased convective heat transfer. Their deterministic nature lends itself to predictive modeling and could result in more consistent structural properties.

For transpiration cooling, as well as in other applications, it is of key importance to be able to predict the fluid transport behaviour of a given design. However, the high speeds and heat fluxes involved make experimental testing cost-prohibitive. This leads to the need for accurate and robust numerical simulation tools to undertake this analysis. This in turn creates a new set of challenges, as conventional computational fluid dynamics (CFD) simulation methods are not well positioned to handle the complex geometries involved in porous media flows.

Furthermore, in the context of additive manufacturing, it is not well understood how as-printed part morphology performs compared to the original design. Significant differences in flow performance may occur due to irregularities in print fidelity and rough surface conditions, which are inherent in metal AM processes. Characterization of these deviations

is essential to creating accurate engineering models for design.

1.2 Objectives

The work detailed in this thesis was conducted with the following major objectives in mind:

1. Develop an analysis framework for conducting CFD simulation of TPMS structures and evaluating the differences between ideal design geometry and real as-printed geometry.
2. Characterize the design space by examining the manufacturability and fluid transport behaviour for various TPMS geometries.
3. Apply this gained knowledge to the design of more complex components with specific performance targets.

1.3 Contributions

The novel contributions within this work are:

- A first attempt at bridging the gap between the distinct fields of metal additive manufacturing and computational fluid dynamics simulation.
- CFD analysis of as-printed part geometry, including a comparative study against the design geometry.
- Application of the devised method to complex parts, showing that the performance differences are non-negligible.
- Development of a computationally straightforward voxel-based method of analysing print fidelity.

1.4 Thesis Structure

This thesis is structured into five distinct chapters. This first chapter serves as a brief introduction to the work. Chapter 2 provides an overview of the relevant manufacturing technologies and numerical methods necessary for understanding of the thesis. It explores the extant body of literature, which are drawn from several disjointed fields of research (transpiration cooling, AM and design, CFD, permeability theory), with the aim of synthesizing a coherent account of the state of the art. Key studies and gaps in the current understanding are identified. Chapter 3 contains the major ideas of the present work. It describes in detail the design and AM fabrication of the structured porous samples and the methodology that was developed to analyse the geometric fidelity of manufactured samples with respect to the ideal design geometry. It presents the results from this analysis and the steps taken to ensure validity of the CFD simulation. Chapter 4 presents an attempt to extend the work from a purely academic sense into an applied setting. It details the creation and simulation of two different leading edge structures using functionally graded TPMS in an attempt to produce non-uniform flow permeability. Chapter 5 concludes the work with an overview of the major findings, potential sources for error, and recommendations for next steps.

Chapter 2

Literature Review

2.1 Transpiration Cooling

The concept of transpiration cooling as a method of thermal protection dates back to the early pioneers of rocketry, including Hermann Oberth and Robert Goddard, who proposed and conducted small scale experiments circa 1930 [4]. More extensive research was performed at various institutions in the 1940s and 50s, but research efforts stalled somewhat due to the lack of suitable materials, inability to fabricate complex porous geometries, and absence of predictive modelling capability. Since the 1990s, renewed efforts have been made, especially with porous ceramic composites [5, 6], experimentation in high-speed shock tunnels [7], and the use of high-performance computing tools [8].

In transpiration cooling, thermal protection is achieved through two complementary mechanisms: convection and film cooling [9, 2]. Coolant passing through the porous material absorbs heat through convective heat transfer, thus cooling the bulk of the material. Additionally, as the coolant exits the porous matrix into the boundary layer, the cooler fluid forms a buffer layer between the hot gas and the outer surface, shielding it from the external heat flux. The coolant is then advected downstream and continuously replaced by new coolant flowing from within the porous material.

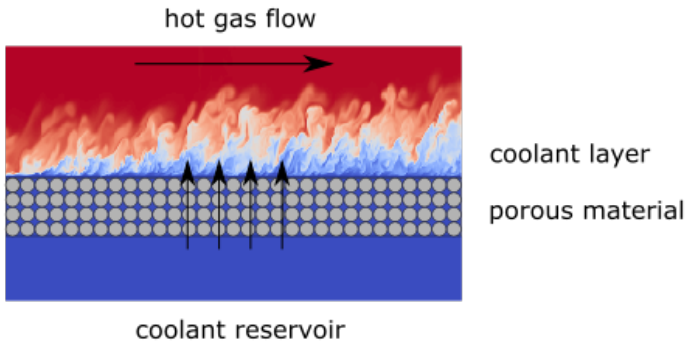

Figure 2.1: Diagram of transpiration cooling (not to scale). Adapted from simulation results by Christopher et al. [10]

Some overlap exists between the terminology of film, effusion, and transpiration cooling. All three methods involve the same principle of injecting coolant fluid into a freestream flow from a solid structure in order to provide thermal protection. Broadly speaking, film cooling uses a single row of discrete holes at the start of the flow to do this. Effusion cooling uses an entire array of holes, and is therefore characterized by lower individual jet velocities, and associated interaction between jets [11]. In terms of coolant hole distribution and size, the demarcation between effusion and transpiration cooling is not well defined. However, a key distinction of transpiration cooling is the additional mechanism of convection heat transfer within the structure itself, prior to interaction with the freestream. Even during the early investigations in transpiration cooling, the effect of heat transfer from the wall structure to the coolant fluid was identified as crucial to cooling effectiveness [4].

It is therefore unsurprising that transpiration cooling has been shown to be more effective than effusion cooling, which in turn is more effective than film cooling. As an aside, the major deficiency with film cooling is the phenomenon of "coolant lift-off". The high jet velocities required for a single row of holes to supply the necessary amount of coolant fluid cause the coolant layer to initially detach from the solid surface, before re-attaching further down. This leads to vortices and an incomplete coolant film over the structure, reducing the coolant effectiveness [11]. Effusion and transpiration cooling circumvent this problem by distributing the coolant injection across the entire surface.

In general, a porous structure with a larger number of coolant holes which are smaller

in size will lead to better theoretical performance, because the coolant flow produces less boundary layer mixing [11]. In practice, however, smaller pores are susceptible to local hotspot-induced failure [2], and in the case of liquid coolants, vapour-locking [11]. This causes a cascading failure that spreads throughout the structure and is catastrophic to cooling effectiveness. The need to properly understand fluid transport behaviour within transpirationally-cooled walls is therefore of great importance.

2.2 Relevance of Additive Manufacturing for Fabrication of Complex-Shaped Metallic Structures

Additive manufacturing (AM) provides an answer to one of the great challenges in transpiration cooling: the need to fabricate complex porous structures. Research and development efforts in AM began in earnest during the 1980s. Since then, it has matured into a promising method of manufacturing and is beginning to see industry adoption not just for rapid prototyping, but for full-scale production of high-performance metal parts [12]. One promising AM process for these types of components is laser powder bed fusion (LPBF).

Laser powder bed fusion, variously referred to as direct metal laser sintering (DMLS) and selective laser melting (SLM), uses a controlled laser that fuses metal powder layer-by-layer according to a CAD model, using a recoater to add successive layers of powder [13]. The build process typically takes place in an inert gas environment to prevent oxidation. A diagram of LPBF is provided in Figure 2.2. A wide range of metal powders can be used for LPBF, and the process can achieve 99+% densification [14]. Post-processing techniques such as hot isostatic pressing (HIP) can bring this up to near complete densification (99.99%) [15], in addition to tailoring the mechanical characteristics [16].

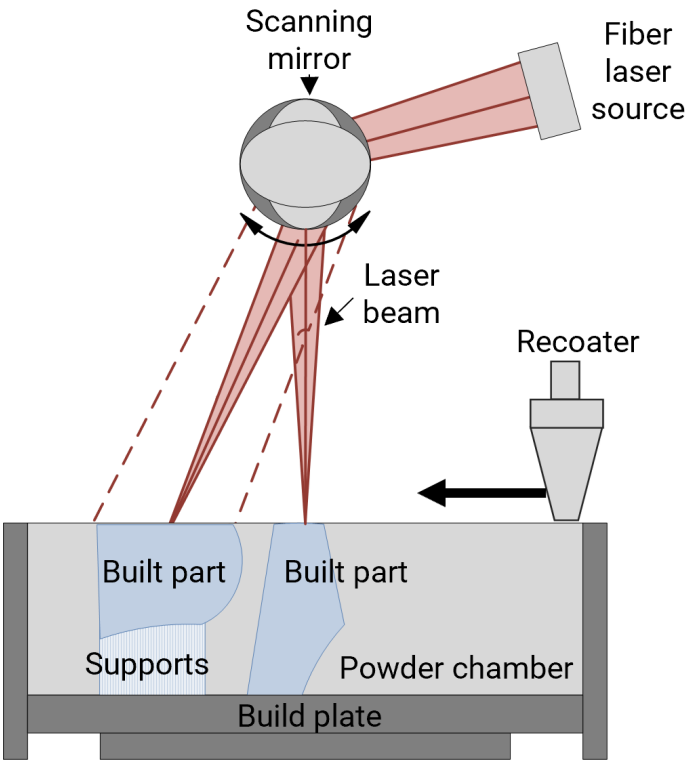

Figure 2.2: Diagram of a typical laser powder bed fusion process.

A similar process to LPBF is electron beam melting (EBM), which uses a focused electron beam in a vacuum environment to fuse metal powder, instead of a laser. EBM can process brittle materials and high-melting point materials, and experiences less oxidation of parts compared to LPBF [12]. However, it is difficult to tune process parameters for, and only a few materials have been characterized for its use, including Ti-6Al-4V and Inconel 718. Another technology of interest is binder jetting AM (BJAM), a sinter-based method that produces parts by sequential layering of metal powder, alternating with selective jetting of a liquid binder to glue particles together to create a green part; green parts are then sintered to densify [17]. EBM and BJAM have found use in production of parts for multiple sectors, including the aerospace and biomedical industries. The primary focus of this thesis is on LPBF, but EBM and BJAM should not be discounted as a viable AM process for producing porous structures.

Although the working principle of LPBF is fairly straightforward, the physics behind the laser-material interaction are highly complex, and significant research efforts have been made towards understanding them. There are many process parameters that can be adjusted to tailor the melting and solidification of the material, including but not limited to laser power and pulse settings, scanning velocity, scanning strategy, powder size/distribution, and layer thickness [13]. All of these affect the formation and properties of the melt pool, solidified layer, and resultant part. Unlike conventional fabrication techniques, the layer-based process of LPBF leads to highly anisotropic grain structures [13]; as well, the rapid fusion and cooling involved produce residual stresses (much like in welding processes). The surface morphology of LPBF-produced parts have non-negligible roughness, which further varies with respect to the surface inclination for three categories of surfaces with respect to the horizontal plane: upskin (facing upwards), sideskin, and downskin (facing downwards) [18]. It is important to note that downskin surfaces at an overhang angle of 45° or steeper typically require support structures to anchor the part to the metal build plate, to prevent part warping and distortion, and to provide a thermal conductivity path to prevent localized overheating (vaporisation) of the material system, as powder itself has poor thermal conductivity properties.

Broadly speaking, many safety and/or performance-critical industries are hesitant to adopt metal additive manufacturing, because the relationships between process parameters and final part quality are not well understood. Much work has been done to model the underlying physics behind LPBF and other AM processes, in order to better predict the properties of the component(s) produced.

2.3 Triply-periodic Minimal Surfaces

Traditional porous materials for transpiration cooling have included partially-sintered metal or ceramic foams [5, 19] and more recently, ceramic matrix composites (CMCs) [9]. These materials can broadly be considered as process-driven structures: their material properties, including porosity, are primarily controlled by the manufacturing process (e.g. feedstock

material, process time and temperature) and are generally stochastic in nature. Prediction of these properties therefore is done through empirical testing, which then leads to models of the manufacturing processes themselves.

The needs of many applications, including transpiration cooling, have spurred the development of "architected" structures, or design-driven materials. In these, the mesostructure is directly prescribed as some form of lattice. While the end product can never be fully decoupled from the manufacturing process, the material properties are nevertheless primarily influenced by the size and shape of the unit cell lattice structure, as well as the feature (wall or strut) thickness.

One such group of these design-driven lattices are the triply-periodic minimal surfaces (TPMS). TPMS structures are space-filling architectures which use mathematical functions to describe their geometry. A TPMS equation defines a smooth, continuous isosurface which demarcates the boundary between solid and empty volumes [20]. These structures are periodic in 3-dimensional space and are typically characterized by long, winding channels. The classical TPMS geometries include the Schoen gyroid, Schwarz diamond, and Schwarz primitive (see Figure 2.3) [21].

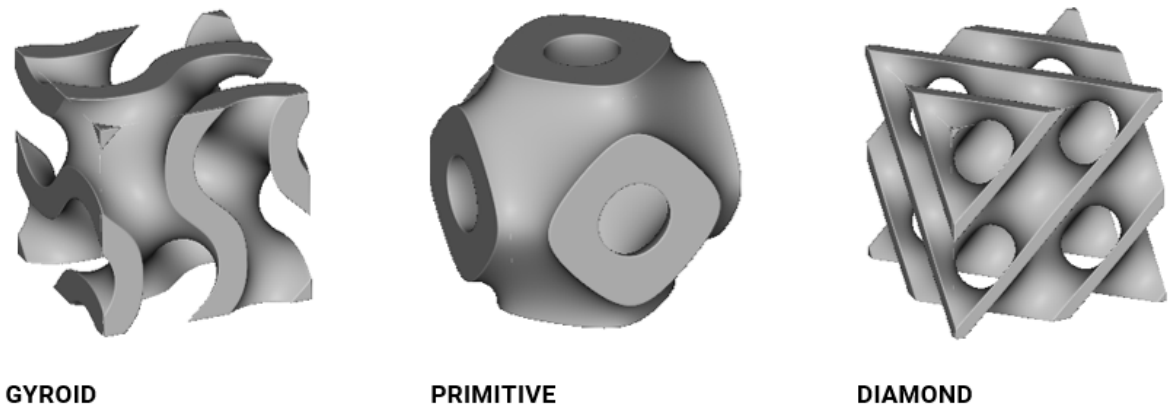

Figure 2.3: Unit cells of the three most common triply-periodic minimal surfaces (gyroid, primitive, and diamond), with non-zero thickness.

Since their development in the 1970s, many other TPMS lattices have been developed. However, because of their structural complexity, impossible to manufacture by conventional

means, TPMS research was relegated to a mostly academic, mathematical endeavour. With additive manufacturing, the ability to fabricate TPMS structures at very small unit cell sizes is now possible.

Currently, the primary applied research thrust for TPMS is in human bone implants. Considerable experimentation has been conducted to determine the properties of TPMS materials in a biomedical context. For bone implants, it is desirable to mimic the elastic modulus and porosity of natural cortical and trabecular bone in order to improve implant longevity [22]. Also, of interest are the fluid flow characteristics through these structures and their impact on bone cell regeneration and growth. This body of work forms the basis for available literature on TPMS structures. The vast majority of metal TPMS structures are fabricated using LPBF. The primary material used for biomedical applications is Ti-6Al-4V alloy, due to its high strength-to-weight ratio, manufacturability, and proven biocompatibility [22].

TPMS structures have the potential to be suitable candidates for transpiration cooling. Their high surface-to-volume ratio [3] compared to other structures of similar porosity could produce increased convective heat transfer. Their deterministic nature lends itself to predictive modeling and could result in more consistent structural properties. Defining a TPMS structure to achieve a target porosity and unit cell size is straightforward due to the mathematical definition of the topology. For example, the Schoen gyroid is defined as the locus of points satisfying the equation:

$$\sin\left(\frac{2\pi}{L}x\right)\cos\left(\frac{2\pi}{L}y\right)+\sin\left(\frac{2\pi}{L}y\right)\cos\left(\frac{2\pi}{L}z\right)+\sin\left(\frac{2\pi}{L}z\right)\cos\left(\frac{2\pi}{L}x\right)-t=0 \qquad (2.1)$$

where the unit cell size L and the wall thickness t can be specified to produce the desired geometry [3]. By varying these parameters, different levels of porosity and fluid permeability can be achieved. This variation can also be applied over a smooth gradient in order to produce a spatially-changing structure, known as "functional grading". This is explored further in Chapter 4.

The applicability of TPMS as an architected meso-structure for transpiration cooling

rests on the ability to achieve similar structural, mechanical and permeability properties as existing porous materials. Performance requirements for transpiration cooling materials vary based on application and industry specifications. These design criteria are generally unavailable in academic literature. This makes it difficult to directly examine if TPMS can meet these requirements. The feasibility of TPMS structures for transpiration cooling is therefore assessed by comparing the reported mechanical, thermal, and fluid flow properties of TPMS with those of conventional transpiration cooling materials.

From a structural standpoint, typical pore sizes found in transpiration cooling literature depend highly on the manufacturing process used and material properties of the porous component. Dickstein et al. [19] developed an optimized and functionally-graded microporous foam for a hypersonic leading edge and noted pore sizes ranging from 190 to 350 μm. This remains about one order of magnitude lower than the current state-of-the-art additively-manufactured metal TPMS, which can have a unit-cell structure around 2-8 mm enclosing open interconnected voids typically down to 500 µm in minimum feature size [23], although rapid advances are being made towards feature size refinement in this field. From a mechanical performance standpoint, studies have shown that the compressive strength of TPMS structures compares favorably to other porous materials. Yan et al. examined Diamond and Gyroid-type Ti-6Al-4V TPMS lattices which exhibited compressive strengths ranging from 4.7 to 1559 MPa depending on the porosity of the component [22]. By comparison, samples of porous carbon fiber-reinforced silicon carbide (C/SiC), another prospective material for high-temperature transpiration cooling applications, demonstrated a compressive strength between 10 to 23 MPa [24].

The LPBF manufacturability of TPMS structures has been studied both through simulation and experimentally-informed approaches. Yang et al. studied the LPBF manufacturability using Ti-6Al-4V for the Schoen Gyroid with a 4.5 mm unit cell size. They reported an average deviation of only $+0.149/-0.046$ mm between the designed and as-built geometry, indicating a high level of manufacturability [25]. The importance of self-supporting topologies has been highlighted [3, 25], since internal supports in lattice structures for LPBF are effectively impossible to remove.

When considering fluid flow performance for transpiration cooling, the rate of coolant injection must be carefully controlled. For example, Gruel et al. [9] state that transpiration cooling of combustion chamber liners for liquid-fuelled rockets is only viable if the coolant mass flow rate does not exceed 0.7% of the engine mass flow rate, in order to avoid a negative impact on engine specific impulse. The coolant mass flow rate depends on the permeability of the material (see Section 2.4.3), the coolant fluid properties, and the operational pressures of the reservoir and the freestream [9]. Because of the strong dependency of fluid behaviour on pore network architecture, customizable TPMS structures, uniquely addressable via AM processes, are of interest to explore for controlling transpiration cooling phenomena.

2.4 Computational Fluid Dynamics Simulation

Until recently, much of the research work in transpiration cooling was experimental. Although test equipment and procedures continue to improve, the inherently extreme operating conditions for transpiration cooling make such approaches prohibitively expensive. On the other hand, numerical modeling using computational fluid dynamics (CFD) can be used to test a wide range of designs and parameters, without the need to manufacture physical parts. Of course, CFD comes with its own set of challenges and limitations.

Numerical modeling of transpiration cooling is difficult due to the highly-complex physics involved. The freestream flow is often super- or hypersonic, but the coolant flow within the porous structure is many orders of magnitude slower. Nevertheless, the two are strongly interrelated. Additional complications are introduced by the presence of liquid-gas phase change [26, 27], combustion effects, foreign gas interaction [28], and compressibility [29], depending on the application.

Within the literature for transpiration cooling, pore-resolved flows are rarely discussed in simulation-based approaches. Most CFD analysis approximates the flow exiting the porous medium with a simple boundary condition, focusing more on the interaction between coolant and freestream. Typically, most researchers model the transpiration zone as

a wall with a prescribed blowing ratio. Often, a no-slip boundary condition is applied to this entire region, which is convenient but not quite physically correct, as a real transpiration surface must necessarily have openings [30]. In 2020, Christopher et al. conducted DNS simulations in which they modelled the transpiration region as an array of "slits" [10]. The fluid exiting these slits was prescribed to have a parabolic velocity profile (i.e. a laminar channel flow).

Various end goals for numerical modeling of transpiration cooling can be envisioned. The gold standard would be a robust coupled-approach that combines the simulation of the internal and external flows. The difficulty of such a task cannot be understated, and it remains an ongoing challenge [8]. Another useful approach is the improvement of the current paradigm of approximating the porous media flow with a boundary condition. Through concurrent efforts to understand the fluid transport behaviour within the porous structure, more accurate parameters can be prescribed for interaction with the freestream flow. Numerical modeling of the flow through porous media, specifically metal additively-manufactured TPMS, is the focus of this thesis.

2.4.1 Navier-Stokes Methods

The fundamental basis for conventional CFD methods are the continuity and Navier-Stokes equations. At their very core, these are merely the conservation laws for mass and momentum, respectively. The continuity equation states that the change in density over time in an arbitrary fluid volume is balanced by the divergence of mass flux for the volume (i.e. the rate of fluid entering or leaving):

$$\frac{\partial \rho}{\partial t} + \nabla \cdot (\rho \vec{u}) = 0 \tag{2.2}$$

where ρ is the fluid density, and $\vec{u}$ is the velocity field. For incompressible flows, density is constant, and the continuity equation simplifies to:

$$\nabla \cdot \vec{u} = 0 \tag{2.3}$$

The Navier-Stokes equations (NSE) are considerably more complex and the interested reader is invited to consult dedicated literature on the subject [31]. For an incompressible flow, a manageable formulation can be given:

$$\frac{\partial \vec{u}}{\partial t} + \vec{u} \cdot \nabla \vec{u} = -\frac{1}{\rho} \nabla P + \nu \nabla^2 \vec{u} + \vec{g} \tag{2.4}$$

where P is the pressure field, ν is the fluid kinematic viscosity, and g is the acceleration due to gravity (and other external forces), if applicable. The Navier-Stokes equations relate the kinematic flow variables to the stresses arising from both pressure and viscosity. For flows with more complex physics, an energy equation and an equation of state are also required to relate thermodynamic variables such as pressure, temperature, density, internal energy, entropy, etc., in order to fully close the system of equations [32].

In a CFD context, this system of governing equations is discretized, and approximations are solved via numerical methods, most commonly using a finite volume method (FVM) [32]. The physical domain is represented by a mesh of control volumes, and a balance is constructed between source terms, sink terms, and fluxes across cell boundaries, in order to maintain the conservation equations. In the vast majority of cases, this results in a matrix equation $Ax = b$, where A is a sparse matrix. Inverting A to obtain the solution variables in x lies at the heart of traditional CFD methods, and efforts are always ongoing to improve this process.

There are several problems with the use of Navier-Stokes methods for simulating fluid flow through porous media.

2.4.2 The Lattice Boltzmann Method

The lattice Boltzmann method (LBM) was developed in the late 1980s based on earlier models of gas dynamics [32]. LBM is built on a solution of the Boltzmann equations which, under certain assumptions, can be recast into the Navier-Stokes equations. While LBM also uses a discrete grid, it does not make any attempt to directly solve the continuity and Navier-Stokes equations, unlike conventional CFD methods. Instead, it uses a bottom-up

approach of modeling a fluid as particles which collide, and tracking their distributions over time. Its fundamental quantity is the distribution function f:

$$f = f(x, \xi, t) \tag{2.5}$$

where x is position, t is time, and ξ is a measure of the microscopic particle velocity [32]. The evolution of this particle distribution can be expressed with the Boltzmann equation:

$$\frac{\partial f}{\partial t} + \xi \frac{\partial f}{\partial x} + \frac{F}{\rho} \frac{\partial f}{\partial \xi} = \Omega(f) \tag{2.6}$$

where F represents external force terms and $\Omega(f)$ is the collision operator [32]. The most common collision operator in LBM is the Bhatnagar-Gross-Krook model (BGK), which "relaxes" the distribution function towards an equilibrium distribution. Subsequently, the Boltzmann equation can be implemented in a discrete form to produce the *lattice* Boltzmann equation, with external forces ignored:

$$f_i(x + c_i \Delta t, t + \Delta t) = f_i(x, t) + \Omega_i(x, t) \tag{2.7}$$

where the subscript i denotes this discretization [32]. c_i is therefore the discrete particle velocity. In essence, this equation dictates that particles at a given location and time move to a new location at the next time step, governed by the velocity c_i and the collision operator Ω_i. This is implemented as a two-step process in LBM:

1. Collision: an intermediate distribution function f^* is calculated for each node using the collision operator and the state of the previous iteration.

2. Streaming: the resulting distribution f^* is propagated to neighbouring nodes to obtain new particle distributions.

This process is repeated until a converged solution is (hopefully!) reached. Through this set of straightforward microscopic interactions, the macroscopic continuity and Navier-Stokes equations can be shown to emerge, and are satisfied [32]. The lattice Boltzmann

method is therefore a very powerful tool for simulating flow problems that conventional CFD techniques struggle with. In particular, LBM is well suited to modeling flow through complex solid geometry. This is primarily due to two factors: parallelization and wall boundary handling. The simplicity of the numerical scheme allows for much greater parallel computation than with traditional CFD, directly reducing the wall-clock time for a comparable simulation problem.

In LBM, it is often sufficient to simply discretize the domain into a uniform structured mesh (i.e. voxels in 3D) and directly apply the boundary conditions to the solid walls. Wall boundaries can be treated as "bounce-back" nodes, such that particles colliding with them are reflected along the incoming direction. This reproduces the classical no-slip boundary condition [32]. Additionally, curved boundaries in LBM are well approximated despite the stairstepping effect caused by voxelization [33]. In terms of TPMS lattices, existing studies have used conventional Navier-Stokes solvers, but only the ideal geometries were studied, and unstructured meshes were used [34, 35, 36]. Indeed, the simulation of as-printed sample morphology (with surface asperities and geometric distortion influenced by the AM process) does not seem currently possible with conventional CFD given the complex irregularity of the boundaries.

There are however some deficiencies with LBM which impact its ultimate viability for simulating transpiration cooling. The canonical LBM uses a low Mach number approximation and therefore is only suited for weakly-compressible flows; significant error is encountered in the supersonic regime and beyond [37]. Recent developments have been made in simulation of highly compressible flows, but traditional Navier-Stokes solvers remain the industry and academic standard for now. As well, thermal flows are difficult to model with LBM [38].

2.4.3 Permeability Theory

The most straightforward measure of fluid transport performance in porous media is permeability, which relates the bulk velocity of the fluid flow through the material to a pressure gradient. Permeability itself is a function of porosity, tortuosity, pore geometry, and pore

connectivity [39], which are design-driven parameters in TPMS structures, and can be also influenced by various manufacturing-driven outcomes such as surface roughness and shape fidelity [40]. The porosity for TPMS structures is taken in this thesis to refer to the volume fraction of void space.

The pore Reynolds number Re_p can be used to characterize the various flow regimes [39] in a porous material. It is defined as $Re_p = \frac{UD}{\nu}$, a function of the kinematic viscosity, ν, bulk fluid velocity (or Darcy velocity), U, and a characteristic length, D, which for porous materials is by convention designated as the mean pore diameter. It is important to note that for TPMS structures the pore diameter is ill-defined, as the void space is instead arranged into channel-like structures. One common method from the literature is to use the size of the largest sphere that can pass through the structure [41]. A great advantage of TPMS structures is that they are deterministic in the nature of their porosity. However, as Clarke et al. [42] note, a distinction must be made between the designed-for void phase in a TPMS structure and the micropores that may occur inside the solid phase if full densification is not achieved in the AM process.

At low Re_p (≤ 1), viscous effects dominate and Darcy's law is used to predict a linear relationship between the pressure gradient and fluid velocity (written as a 1D equation):

$$-\frac{dP}{dx} = \frac{\rho\nu}{\alpha}U \tag{2.8}$$

where α is the Darcian permeability of the porous media and is in units of area. At higher Reynolds number, as found in most transpiration cooling applications [9], Darcy's Law is inadequate as it does not account for the inertial effects. The Darcy-Forchheimer model accounts for these effects:

$$-\frac{dP}{dx} = \frac{\rho\nu}{\alpha}U + \rho\frac{1}{\beta}U^2 \tag{2.9}$$

where β is another permeability coefficient, termed the drag or Forchheimer coefficient, with units of length. The Forchheimer model has been found to work well for incompressible fluids within the range $1 < Re < 10$. This would apply to the use of liquid

water as a coolant fluid, for example. Greuel et al. proposed a further modification for gaseous coolants at high pressures, where compressibility effects are non-negligible [9]. The permeability coefficients α and β are often considered constant and are determined experimentally for each porous medium [9]. In the present work, only the Darcy permeability α is considered through the study of low-Reynolds number flows, in order to provide a simple starting point for assessing the difference between ideal and as-printed TPMS geometries.

$$Re = \frac{UD}{\nu} \tag{2.10}$$

However, there is disagreement over the relative performance of TPMS structures. Out of the three common TPMS structures (gyroid, diamond, primitive), the Schwartz primitive geometry has been shown to have the highest permeability at porosities $> 50\%$, due to its straight line paths for fluid flow [43][39]. Furthermore, Jung and Torquato put forth the conjecture that, for a porosity of 50%, a TPMS with the lowest surface-to-volume ratio will have the maximal fluid permeability [43]. However, Ali et al. reported that the gyroid topology was more permeable than the primitive at a porosity of 80%, seemingly in direct contradiction to the other findings.

Concerns also arise with the high tortuosity of TPMS structures compared to stochastic porous media. On the one hand, highly tortuous flow paths may lead to increased convective heat transfer, which would provide an advantage over conventional porous media. However, it may also cause large variation in the effective flow regime within the TPMS structure, which could lead to non-uniform coolant dispersal and the development of localized failure.

2.5 Summary

The field of transpiration cooling research has broadened significantly since its inception. New technologies, materials, and analysis methods continue to be incorporated. In the present work, the use of TPMS structures, metal additive manufacturing, and lattice Boltzmann method CFD are explored.

The feasability of TPMS structures for transpiration cooling depends on their ability to be manufactured with the high level of feature resolution required, as well as the repeatability of this process. The TPMS structures examined thus far provide a foundational understanding of the general design space.

The question of material permeability must be examined in a practical context. Increasing permeability leads to reduced pressure losses. Indeed, this is desirable for certain applications of TPMS structures, such as heat exchangers and porous media burners. However, for transpiration cooling, if the permeability of a TPMS structure is too high it may be impossible to limit the coolant injection ratio to an acceptable value. It is uncertain purely based on a review of the literature if TPMS structures can have a low enough permeability to be viable for transpiration cooling, while still being manufacturable.

This thesis work aims to provide insights into the use of AM produced parts for transpiration cooling and other porous media applications. There is a gap in the current literature on CFD analysis of manufactured parts, partially due to the difficulty in applying conventional Navier-Stokes CFD techniques to complex AM geometries. In the present work, the lattice Boltzmann method is explored as a feasible approach, with a focus on studying as-printed part geometry.

Chapter 3

Assessment of design parameters on flow performance[1]

3.1 Motivation

To develop a better understanding of fluid flow behaviour through additively-manufactured parts, three facets of knowledge are necessary. First, a designer requires a streamlined and intuitive method of conducting predictive modeling on potential designs. Triangular-mesh based STL (stereolithography) files, while often necessary for the printing process, are computationally bulky and do not lend themselves well to CFD simulation or to geometric analysis. A voxel-based method would be a significant improvement in this regard.

Second, a characterization of the design space must be made. Within the class of TPMS structures alone, there are several methods of generating unique geometries, including the TPMS type, unit cell size, and wall thickness. While this thesis is not intended to be a comprehensive library of such design choices, the work herein demonstrates the impact of changing these variables on the fluid flow performance, using the aforementioned analysis techniques.

[1]Portions of this chapter are reproduced in a paper submitted to the Journal of Materials Engineering and Performance, under review, titled: "An analysis framework of additively manufactured deterministic porous structures for transpiration cooling", by Zhang, K., Hickey, J.P., and Vlasea, M.

Lastly, it must be recognized that printed parts will perform differently from design due to inherent irregularities in the additive manufacturing process. Therefore, a designer must have a clear idea of the magnitude of this deviation.

3.2 Methods

Figure 3.1 provides a broad overview of the analysis method used in this thesis to study the designed and as-printed geometries for various TPMS lattice structures.

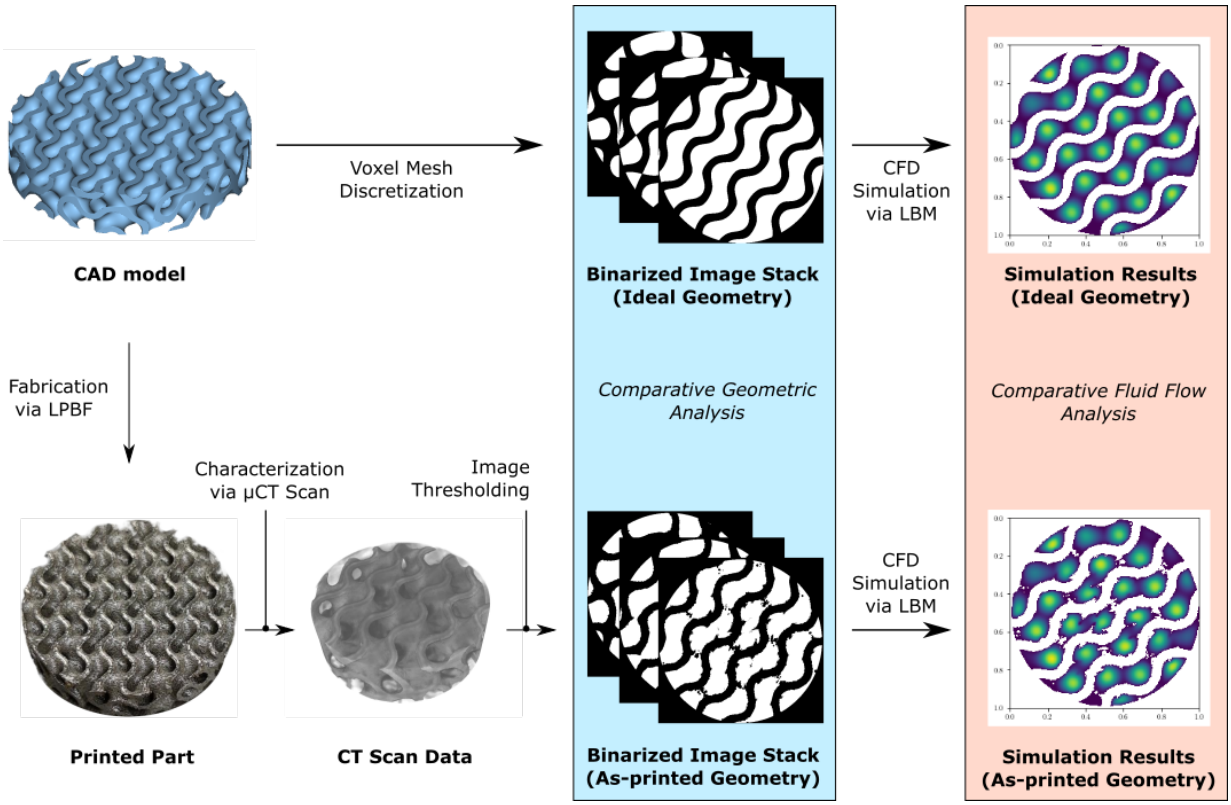

Figure 3.1: Workflow for the comparison of as-printed and as-designed TPMS parts.

3.2.1 Model Generation

For this study, a series of gyroid lattice-based designs were selected to demonstrate the concepts herein. The gyroid architecture is known to have a high specific surface area compared to other TPMS geometries [43, 41]. The increased surface area provides a good opportunity to observe differences between the design and as-printed geometry.

Computer-aided design (CAD) models of the TPMS lattices were generated using nTopology (v3.13.4, New York, United States), an additive manufacturing (AM) design software. Four lattice structures were considered, with varying unit cell size and wall thickness (see Table 3.1). The unit cell for each structure was then prescribed inside a cylindrical volume of dimensions 25 mm diameter and 5 mm height. The lattice design features were selected to ensure manufacturability based on prior work related to LPBF of similar designs [44, 45, 46], and to demonstrate the simulation workflow; they were not specifically optimized for permeability and fluid flow.

Table 3.1: Geometric details of the gyroid disk designs.

Design	Unit cell size [mm]	Wall thickness [mm]	Porosity [%]
Design 1	5.0	1.0	61.0
Design 2	4.0	1.0	49.7
Design 3	3.0	1.0	33.2
Design 4	2.5	0.5	59.6

3.2.2 Part Fabrication

The material used in this study was Inconel 625, a high-performance metal alloy with excellent mechanical properties [47] and corrosion resistance, even at elevated temperatures [48]. Inconel 625 has found use in gas turbine components and combustion chamber linings [49], and thus is well suited for some transpiration cooling applications at lower thermal loads. The powder particle size was between 15-45 µm. The samples were fabricated using a modulated 400W beam laser powder bed fusion (LPBF) system (Renishaw AM400, Renishaw, Wotton-under-Edge, UK) using the nominal beam spot radius of 35 µm and a constant layer thickness of 30 µm. Details on the process parameters for the core and skin of the part are given in Table 3.2. The process parameters for Inconel 625 were selected as the default parameters recommended by Renishaw for latticed architectures. Due to the interplay between the material-laser-design, there are different boundary conditions which need to be considered in selecting process parameters. The core (internal surface within a printed region in a layer) will have a powder layer with a solidified region present under-

neath, while the border (region adjacent to the perimeter of the part), up-skin (inclined surfaces, facing upwards), and down-skin (inclined surfaces, facing downwards) will experience a different boundary condition with respect to the presence of powders and solidified substrate as a function of surface inclination. These regions will require tailored process parameters to ensure manufacturability, acceptable surface quality, and good geometric fidelity; such parameters were successfully used in the past for printing lattice architectures for this material system and were also used in this study; optimization of such parameters is beyond the scope of the present work. Due to the smooth, continuous nature of TPMS structures, no supports were required during the printing process.

Table 3.2: Process parameters for production of the disk samples via LPBF.

Parameter Class	Laser Power [W]	Exposure Time [s]	Point Distance [µm]	Hatch Distance [µm]	Contour Distance [µm]
Core	120	100	80	70	—
Border	90	80	60	50	80
Up-skin	100	110	55	70	—
Down-skin	90	80	80	110	—
Down-skin border	60	70	50	—	—

3.2.3 Characterization via XCT Scanning

The additively-manufactured samples were characterized using a X-ray computed tomography (XCT) scanner (ZEISS Xradia 520 Versa) using voltage and power settings of 160 kV and 10 W, respectively. The voxel size was 15 µm for the raw data. The XCT data was then post-processed using Dragonfly (v3.0, Object Research Systems, Montreal, Canada), an image processing suite. The usable data from the XCT measurements was a cylindrical volume with a diameter of 15 mm and thickness of 4.35 mm, taken from the approximate center of the printed part. The CAD models created in nTopology were trimmed to only include this partial region of the sample. This process of registration (i.e. alignment) of the two volume datasets was necessary to ensure that the CT scan data properly represented the design geometry. It is recommended that future research work use reference features

(i.e. datums, fiducials) in the design to help align the datasets.

Otsu's method [50] was used to threshold the greyscale CT data in order to segment the solid and void regions (see Figure 3.2). This was then exported as a stack of black and white image files, and converted into a binary data file using a MATLAB script for input into the CFD simulation. The CAD model was sliced in nTopology to produce another image stack which was also further processed in MATLAB.

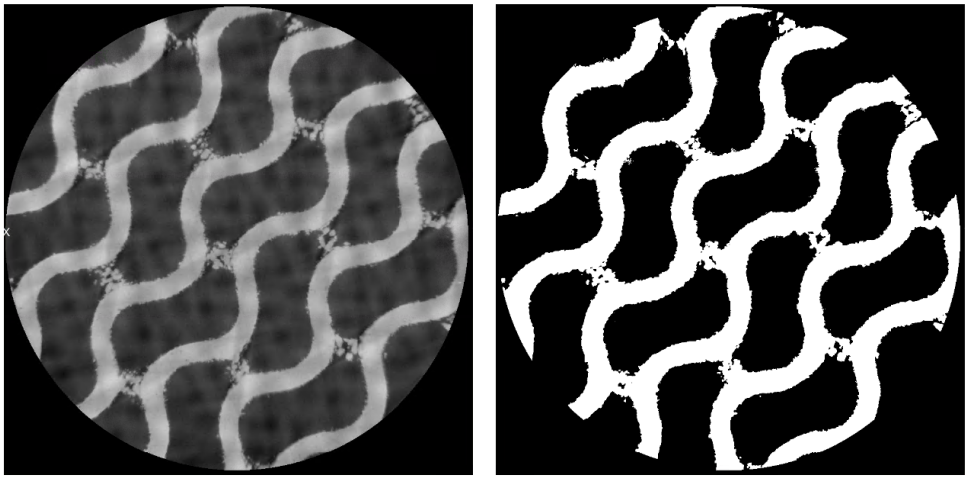

Figure 3.2: Example of Otsu thresholding on one slice of the gyroid disk CT data.

3.2.4 Geometric Deviation

The use of a voxel-based representation for the part geometry leads to a straightforward comparison of the CT-scanned structure to the original CAD design, once the two volumes are properly registered. By comparing each individual voxel from one dataset to the other, it is possible to quantify print fidelity, as well as to obtain bulk volume statistics. Two measures of print inaccuracy were defined: percent overprint and underprint. Overprint is the total count of voxels in which the CT data shows solid material while the CAD data does not (i.e. material present where not expected), normalized by the total number of solid voxels in the CAD. Conversely, underprint is the voxel count for which the CAD shows solid and the CT does not (material not printed where expected), again normalized by total solid CAD volume. The overprint and underprint metrics highlight the actual divergence in shape fidelity, but are affected by registration errors between the two volumes.

In literature, there are numerous ways to assess quality metrics for additively manufactured lattices, with relevance to strut-based lattices [51, 40] and surface-based lattices [52], including assessment of lattice continuity, sub-surface voids or porous defects entrapped in the solidified material system, and surface roughness. For the purpose of this work, the overprint and underprint quantitative data, along with visual assessment of the CT data overlaid with the CAD data were considered to be in scope, with future automated quantitative metrics being considered.

3.2.5 LBM Simulation

Comparative computational fluid dynamics (CFD) simulations of the *as-printed* (also termed CT) and *as-designed* (also termed CAD) TPMS structures were undertaken. To adequately model the complex boundary of the porous material, a lattice Boltzmann method (LBM) is used. The LBM simulations were conducted using an open-source C++ library known as Palabos (https://palabos.unige.ch/) [53]. Details of the numerical method are presented in Table 3.3. Using a 15 µm voxel size for both the as-designed and as-printed cases, the simulation domain was discretized into 290 million grid cells. Of this, the actual fluid domain was about 140 million cells for the CAD geometry and 138.5 million cells for the CT geometry. The basic D3Q19 model was used for the fluid cells (D3 represents three-dimensional, and Q19 represents the number of velocity vectors calculated per grid cell). This model was selected as it was considered the optimal balance between accuracy and computational cost, compared to other LBM models such as D3Q15 and D3Q27 [54, 55]. Simple bounce-back was used for the solid walls. The region outside of the cylindrical volume was also treated as solid, in order to replicate an experimental setup for future work. To drive the flow across the porous medium, a pressure difference of 5.4×10^{-3} Pa was imposed across the domain in the streamwise direction. A summary of the boundary conditions and physical dimensions is given in Figure 3.3. In this work, physical units are used for clarity, to avoid the complexities of unit conversion within LBM; interested readers are referred to dedicated literature on the topic [32, 53].

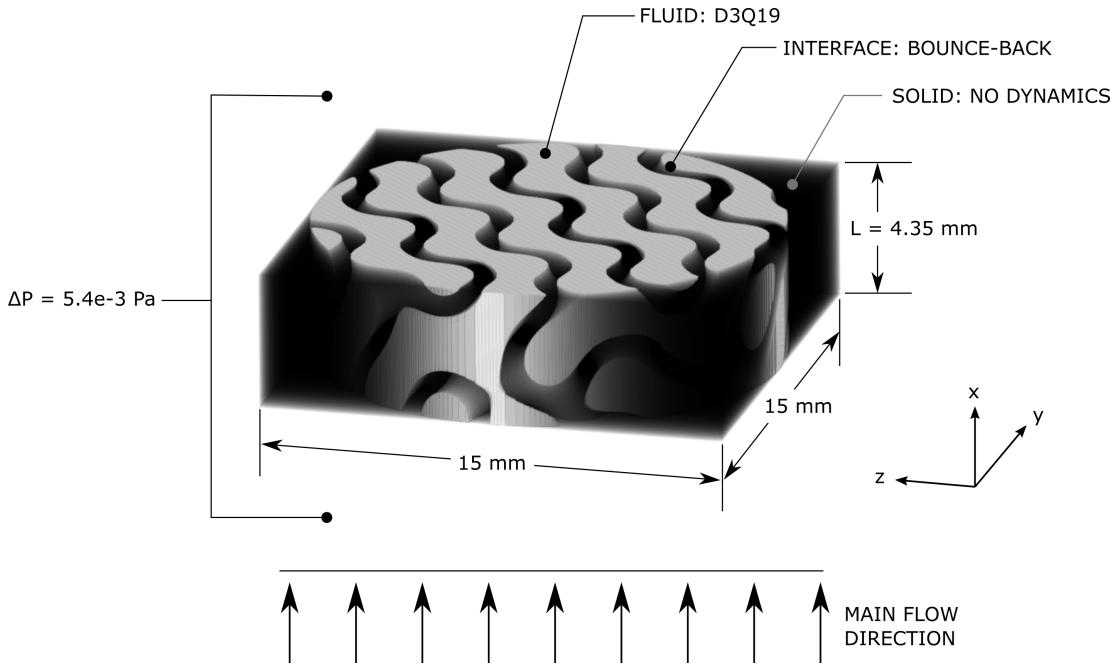

Figure 3.3: Boundary conditions and domain characteristics for the porous disk LBM simulations.

Based on the defined boundary conditions, the simulations were run until a converged steady state solution was reached. The Darcy velocity and permeability were then computed; the results are presented in the following section. Based on the prescribed setup, the pore Reynolds number ranged from approximately $Re_p = 0.03$ to $Re_p = 0.24$ for the different geometries, thus satisfying the condition for laminar Darcy flow. The pore size was defined based on the diameter of the largest sphere that could pass through the structure; the pore size was estimated to vary between 0.8 mm. and 1.8 mm.

Table 3.3: Parameters for the LBM simulation.

Lattice model	D3Q19
Collision operator	SRT-BGK
Relaxation parameter τ	1.0

3.3 Results and Discussion

3.3.1 Geometric Analysis

Detailed results are explained below for disk Design 1 (with a 5 mm unit cell size). Aggregate results for the entire set of geometries are presented afterwards. For Design 1, the measured bulk porosity of the CT-scanned volume was 60.4%, which was very close to the target CAD porosity of 61.0%. The total overprint was 21.3% and the total underprint was 19.9%. Because the bulk values of overprint and underprint were very similar, while the porosity values were nearly identical, an initial suspicion was that the dataset registration was flawed (i.e. that there might have been a degree of shifting between the two volumes) due to user error during manual alignment. Further analysis shows that this is not the case, however. Figure 3.4 shows the CT data superimposed over the CAD model, where the overprinted regions are visible.

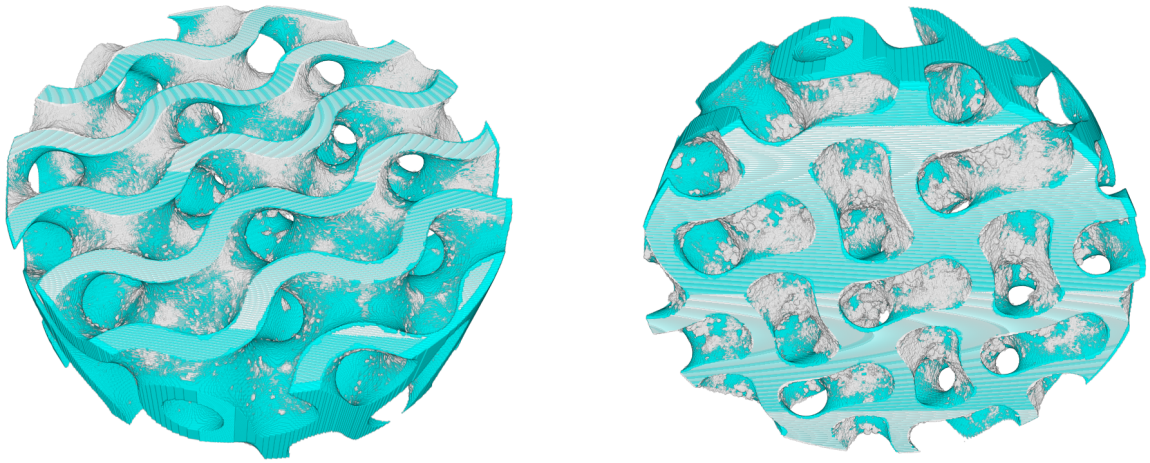

Figure 3.4: Superimposition of the as-printed (grey) and ideal (blue) sample geometry, showing the upskin (on left) and downskin (on right) surfaces.

The divergence in shape fidelity can be attributed to a variety of manufacturing-related factors such as, but not limited to, the resolution of the surface tesselation in the source file, stairstepping effects introduced by the layer thickness, feature distortion due to cyclic thermal loading and induced residual stress, surface roughness dependency based on the

angle of inclination of the surface, the island-effect of two volumes joining within a layer, and the direction of powder spread and chamber gas flow [56, 57]. In the present sample, the overprint is much more pronounced on surfaces that are downward-facing with respect to the build direction, also called downskin; this is typical to the LPBF process due to the laser-powder interaction phenomena [18]. To provide some further insight, the overprint and underprint were recalculated on a layer-by-layer basis. The results are given in Figure 3.5.

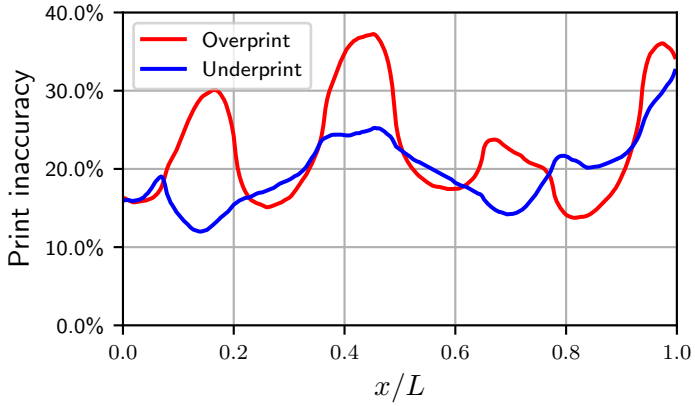

Figure 3.5: Measures of print geometric deviation calculated on a layer-by-layer basis for Design 1.

Because the overprint and underprint curves are sufficiently different (they do not track one another nor are they phase shifted), and based on visual inspection of the superimposed datasets in Figure 3.4, we believe the geometric deviation of the the printed part to be overall representative of expected quality in LPBF, with minimal error contributions from the manual registration process of the two datasets. Table 3.4 shows the geometry analysis results for all four designs. The remaining layer-by-layer graphs are provided in Appendix A.

Table 3.4: Geometric fidelity analysis of the four disk designs.

Design	Target (CAD) Porosity [%]	Actual (CT) Porosity [%]	Overprint [%]	Underprint [%]
Design 1	61.0	60.4	21.3	19.9
Design 2	49.7	51.6	6.5	10.2
Design 3	33.2	37.0	4.4	10.0
Design 4	59.6	60.0	36.7	37.6

3.3.2 Fluid Flow Analysis

The LBM simulations of the as-printed and as-designed parts are compared by normalizing the computed velocity by the Darcy velocity, U_0, of the as-designed case. Again, only Design 1 is presented in detail, with the bulk results given afterwards. Velocity distribution at three characteristic planes of both cases are given in Figures 3.6 and 3.7. The velocity distribution shows many similarities in the bulk properties of the as-printed and as-designed parts despite the obvious additional wall roughness effects in the as-printed part. To compare the impact of wall roughness on the permeability of the porous structure, the Darcy permeability was calculated. As anticipated, the as-printed geometry had a lower permeability ($2.47 \times 10^{-8}\,\mathrm{m}^2$) compared to the ideal design ($2.90 \times 10^{-8}\,\mathrm{m}^2$), a decrease of 14.8%.

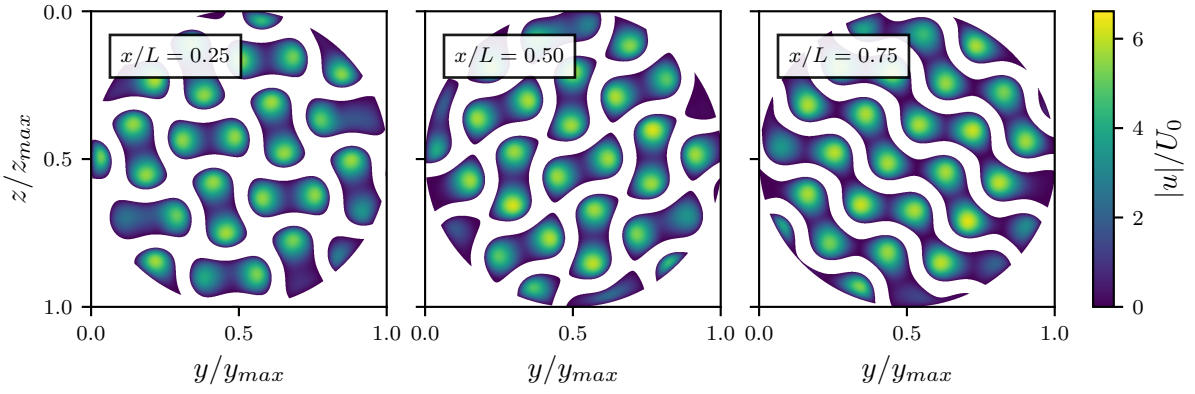

Figure 3.6: Velocity magnitude profiles at three cross-sectional locations for the CAD data of Design 1.

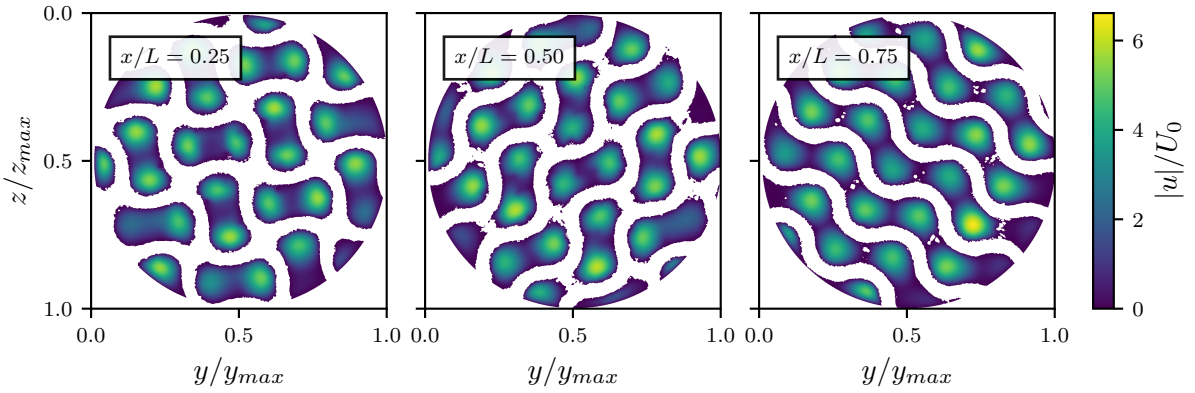

Figure 3.7: Velocity magnitude profiles at three cross-sectional locations for the CT data of Design 1.

As expected, the bulk velocity through the as-printed part was lower, for the same imposed pressure gradient, due to the non-ideal surface morphology. This can be seen in the mean velocity at each depth throughout the sample thickness (see Figure 3.8). For the streamwise (i.e. major flow direction) velocity component u, the CT case follows the same periodic trend as the CAD case, but at a lower overall velocity. However, for the two other velocity components v and w, the CT case is roughly similar compared to the CAD case.

To gain some further insight, the root-mean square (RMS) of the velocity (i.e. the square root of the velocity variance) was computed for each streamwise location throughout the sample (see Figure 3.9). The spatial velocity variance of the CT case is lower than in the CAD case, and both follow the same trend in all three flow directions.

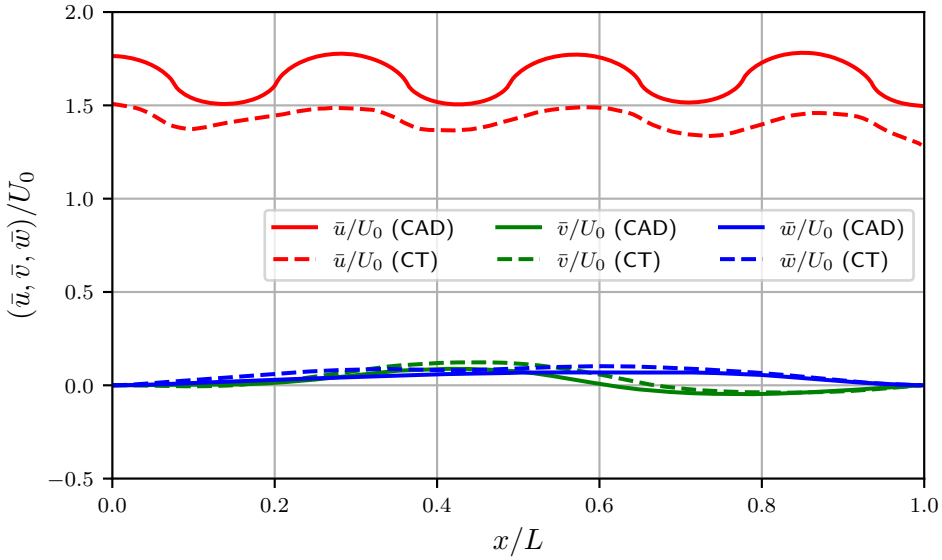

Figure 3.8: Mean velocity component profiles for Design 1.

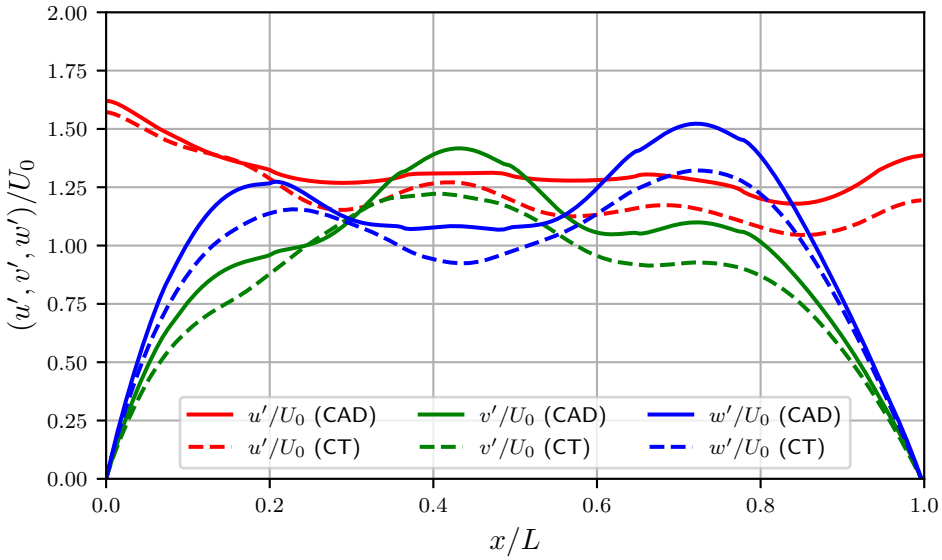

Figure 3.9: RMS velocity component profiles for Design 1.

The flow through both geometries develops into snaking pipe-like structures along the paths of "least resistance" (see Figures 3.6 and 3.7), with a parabolic velocity profile in these regions, and stagnation elsewhere. Within these structures, the CT case exhibits lower peaks in flow velocity than the CAD case, causing the RMS velocity for any given

region to be lower.

Further evidence for this difference in flow behaviour can be seen in the distribution of velocity magnitude for each case (fluid domain only), given in Figure 3.10. The CT case shows significantly more instances of grid cells with zero velocity, corresponding to the increased wall surface area at which the no-slip boundary condition is imposed. This influences the rest of the flow domain, leading to a higher occurrence of lower velocity values ($|u|/U_0 < 3$) and fewer peak values. As expected, the CAD geometry has a greater occurrence of higher velocity events.

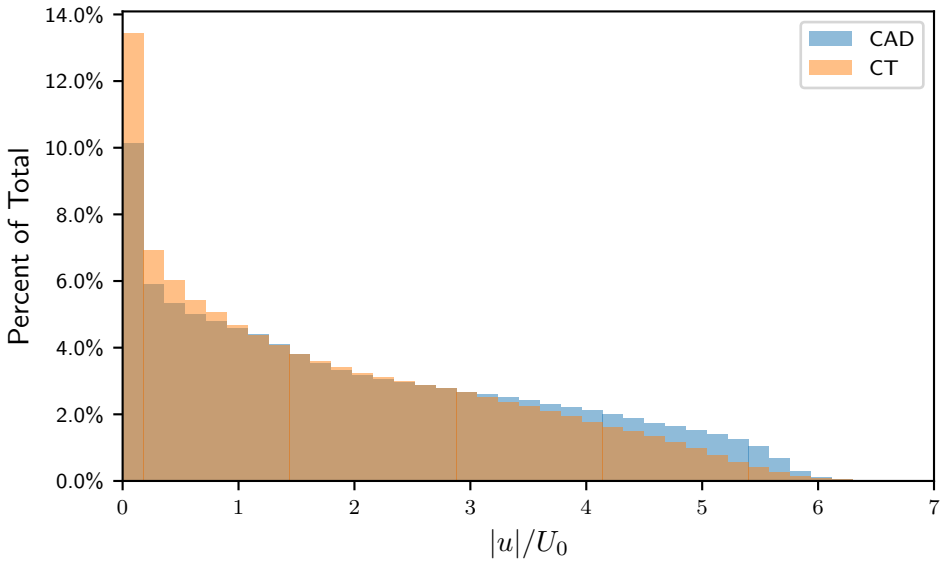

Figure 3.10: Comparison of velocity magnitude distributions for Design 1.

The flow behaviour in the as-printed case agrees well on the whole with that of the ideal geometry, with both the mean and RMS velocities following the expected flow evolution. For brevity, the mean and RMS velocity plots for the remaining samples are provided in Appendix B. The overall permeability results for the entire set of samples are presented in Figure 3.11.

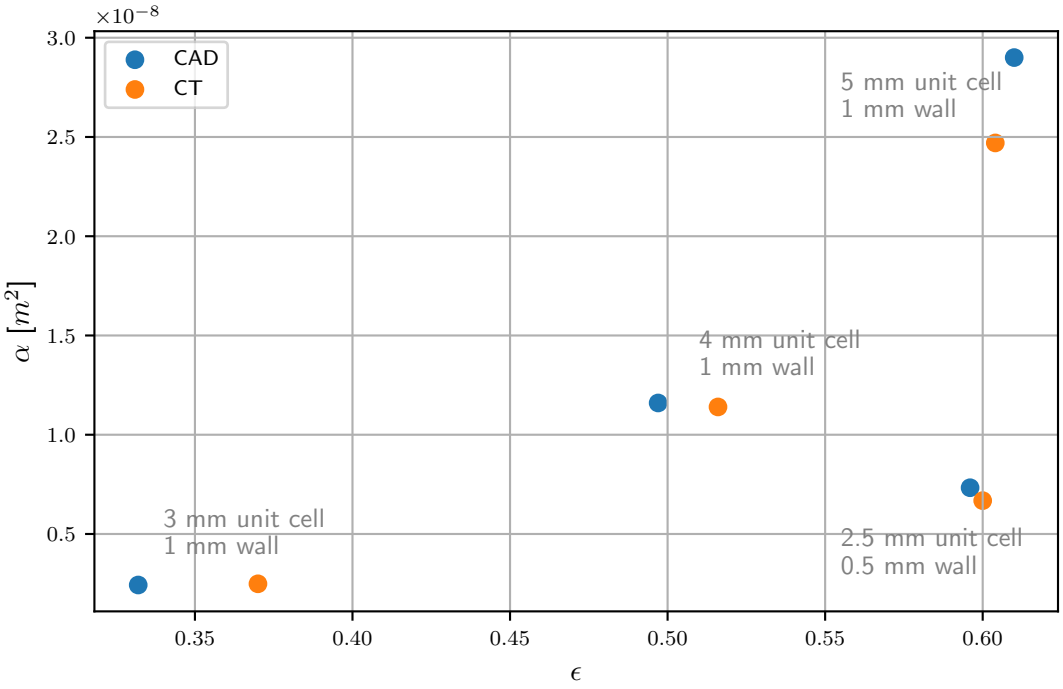

Figure 3.11: Permeability vs porosity for the gyroid disk samples.

The overall trend of the results is reasonable. An decrease in unit cell size leads to a decrease in permeability, as the pathways for fluid flow become smaller/more constricted. This behaviour is not a strict function of porosity, however. Design 1 has approximately the same porosity as Design 4, but the latter has a significantly lower permeability. This suggests that fluid permeability is more accurately related to pore size.

The explanation for the behaviour between the as-designed and as-printed parts is less clear. Since the printed surface morphology is coupled to the printing process, the surface quality was expected to be the same (or worse) as the feature resolution became finer (i.e. more difficult to print). Such imperfections would then constitute a larger proportion of the overall structure for smaller unit cell sizes. It was therefore hypothesized that this would result in increased losses. This was not strictly the case. The samples with smaller unit cell sizes (except for the 2.5 mm sample) indeed exhibited greater print deviation, but the simulated permeability was actually closer to the design than for the 5 mm unit cell sample. One possible explanation is that the effect of overall underprinting (which increases the

bulk porosity) counteracts the proportionally-higher state of surface roughness.

Unfortunately, the number of samples tested was insufficient to make any conclusive statements, but the results highlight the dangers of neglecting actual as-printed part behaviour during the design process. It is important to also note that there is ongoing research focused on surface modification of printed lattice architectures [58] to increase geometric fidelity of printed structures, further increasing the confidence in design refinement, simulation workflows, fabrication and post processing of such designs towards adoption in transpiration cooling applications.

Ultimately, transpiration cooling systems are assessed on their heat transfer efficiency, while the analysis presented focused on flow velocity as a first step. There are several ongoing challenges facing the development of a LBM thermal simulation for transpiration cooling. The thermal boundary conditions depend both on the internal solid phase conduction and external fluid convective heat transfer within the boundary layer. The assessment of these parameters requires the consideration of conjugate heat transfer which is currently a topic of active research with lattice Boltzmann methods [59, 38]. As well, the resolution required to adequately capture the thermal boundary layer within the TPMS structure, especially for the as-printed part, would be challenging to capture given the resolution of the voxelization.

A final note is that, generally speaking, in the presence of surface roughness or any non-smooth geometric changes, the simulation residuals will take longer to converge, increasing the overall run time. However, this was not the case for the simulations: both the as-printed and as-designed cases took approximately the same number of iterations to converge. This suggests that the influence of the as-printed surface morphology is captured in earlier iterations, which may be a strength of LBM over conventional CFD methods.

3.4 Validation of Method

To validate the simulation method, a number of test cases were first studied:

1. laminar Poisseuille (pipe) flow

2. infinite array of packed spheres

3. cubic gyroid TPMS array (from Pires et al. [36])

These validation cases were selected to incrementally build confidence in the simulation method. Each test geometry was similar in size/length scale to the TPMS structures of interest. As well, a mesh refinement study was performed to ensure that the TPMS simulation results were grid-converged (see Appendix C).

3.4.1 Poisseuille Flow

The code was first used to simulate the classical case of a laminar Poiseuille flow (through a straight cylindrical pipe), which has an analytical solution [60]. The velocity profile for fully-developed flow is a paraboloid with the equation:

$$u(r) = u_{max}\left(1 - \frac{r^2}{R^2}\right); \qquad u_{max} = -\frac{\Delta P}{L}\frac{R^2}{4\rho\nu} \tag{3.1}$$

where r is the radial coordinate, R is the pipe radius and L is the pipe length. The average (or Darcy) velocity U_0 is also analytically known to be equal to $u_{max}/2$. A short section of pipe geometry was implemented in Palabos, corresponding to physical dimensions of 12.5 mm radius and 100 mm length. A pressure delta of 4.88×10^{-5} Pa was imposed across the length of the pipe. Three grid resolutions were tested: $25 \times 25 \times 100$ cells, $50 \times 50 \times 200$ cells, and $250 \times 250 \times 1000$ cells.

The LBM implementation was able to perfectly reproduce the fully-developed velocity profile, even with the most coarse grid resolution (see Figure 3.12). The Reynolds number was calulcated to be $Re = 1.21$, well below the threshold of $Re < 2300$ for laminar Poiseulle flow [60]. One observation is that the pressure boundary condition used does not impose any fixed velocity profile at the start or end of the domain, and thus entrance length effects are not considered.

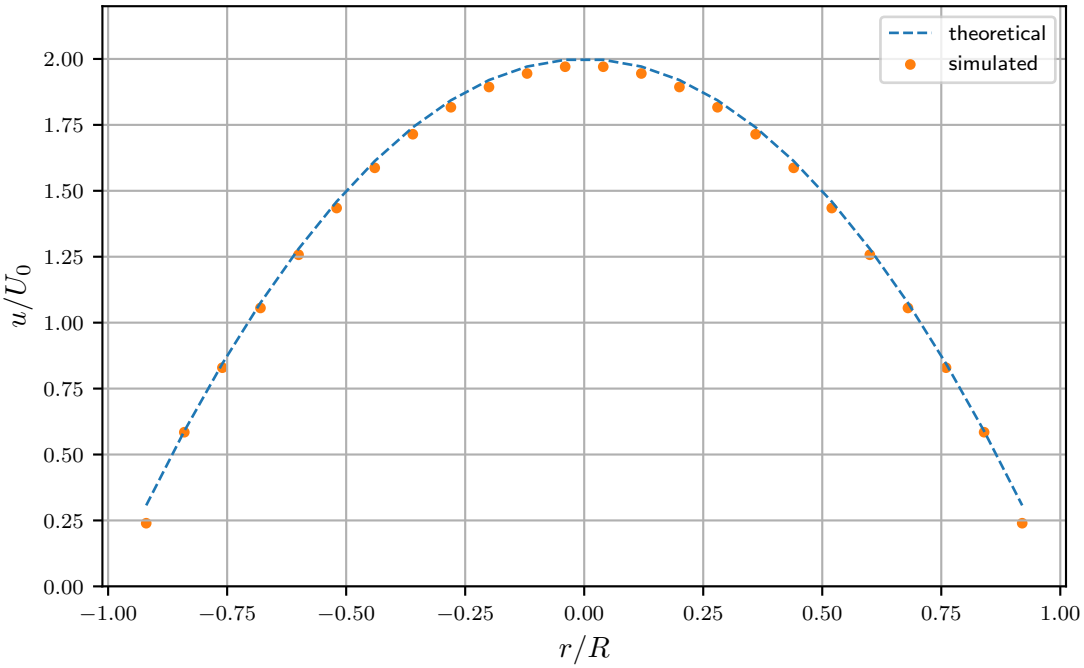

Figure 3.12: Validation of LBM simulation on a straight pipe flow. Simulated velocity profile versus analytical solution.

3.4.2 Packed Spheres

The next case that was tested was the canonical Stokes flow through an infinite array of packed spheres. The periodic arrangement of a cubic unit cell with a centrally fixed sphere produces the simple cubic packing, which has a maximum solid volume fraction of $\phi = \frac{\pi}{6} \approx 0.524$. Zick and Homsy [61] derived the analytical solution to the relationship between pressure gradient and mean flow velocity for any given volume fraction ϕ under Stokes flow:

$$\frac{\Delta P}{L} = \frac{9}{2}\frac{\rho\nu}{a^2}\phi K U_0 \tag{3.2}$$

where L is the cube edge length, a is the sphere radius, and K is an analytically-determined drag coefficient. To simulate this flow, a unit cell with 10 mm edge length and a central solid sphere of variable diameter was constructed. This was then simulated in

Palabos, using a mesh size of $60 \times 60 \times 60$ grid points. A periodic boundary condition was applied in all three coordinate axes, and the flow was driven by a pressure difference of 1.76×10^{-3} Pa. The simulation results were recorded and used to calculate a K value for various volume fractions. These were then compared against the analytical values (see Figure 3.13). The results match fairly well, but some deviation is observed as volume fraction increases.

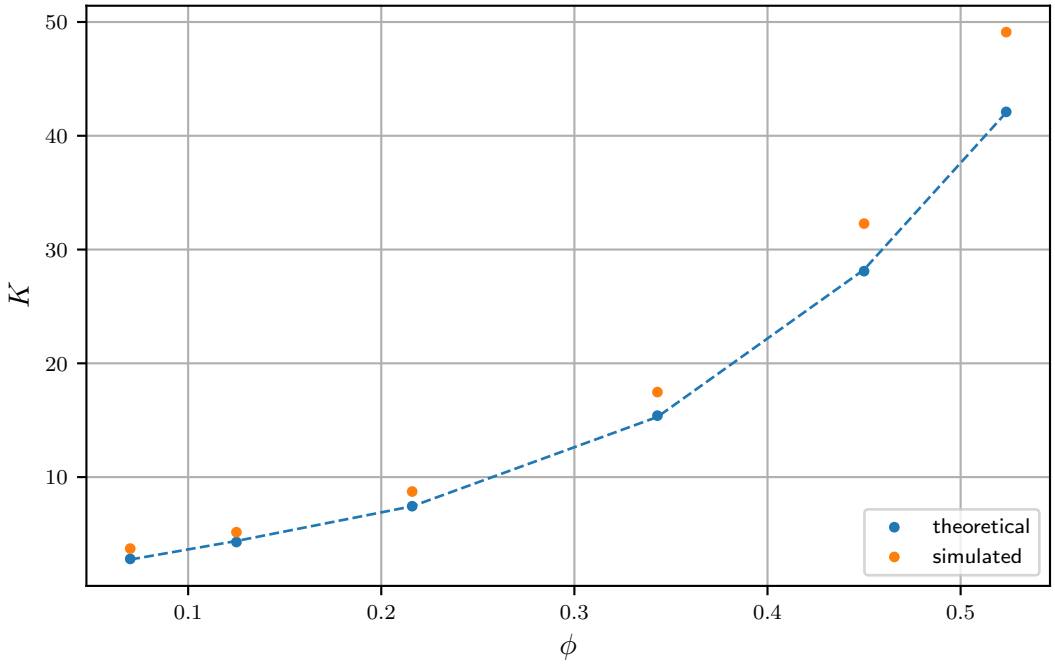

Figure 3.13: Validation of LBM simulation on an infinite array of packed spheres. Drag coefficient K versus volume fraction.

3.4.3 TPMS from Literature

A number of simulations were then performed based on the numerical and experimental work of Pires et al. [36]. A cubic gyroid lattice of 60% porosity was recreated from this literature and simulated with LBM under the same test conditions. The results from the LBM method were similar to the numerical results by Pires et al. (done with a conventional CFD solver), but both are significantly different from the experimental results (see Figure 3.14).

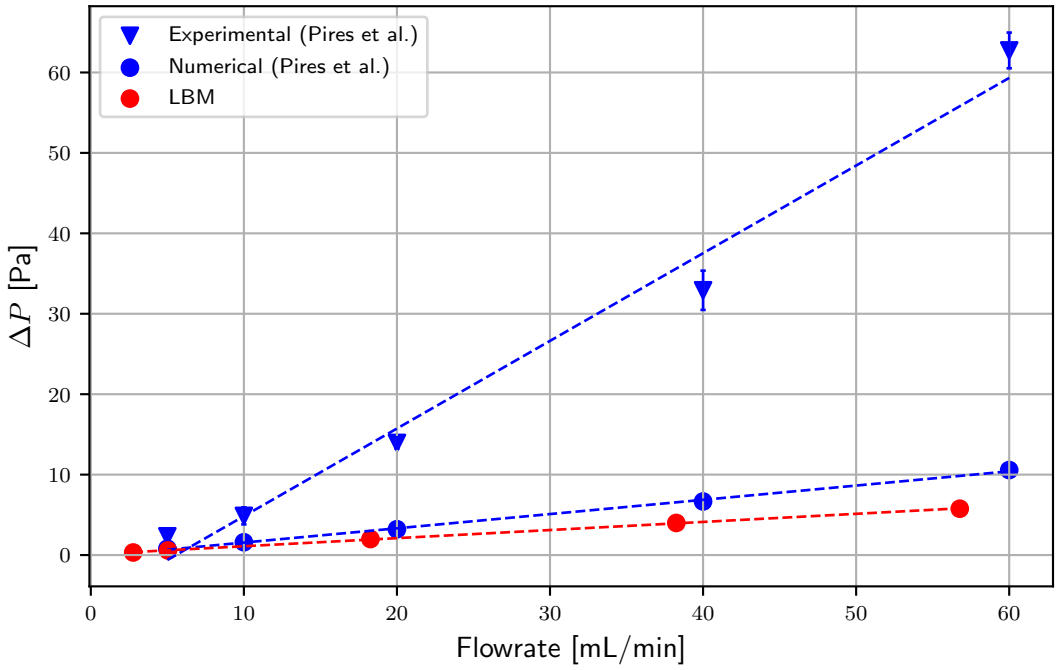

Figure 3.14: Validation of LBM simulation showing pressure drop versus flowrate for the SG60 sample from Pires et al. [36]

This suggests that the current CFD approaches, regardless of method, are missing some fundamental physics related to TPMS structures. Further investigation is needed to study this *absolute* discrepancy, but the validity of the *comparative* results between CFD simulation of ideal and as-printed geometry presented herein can still be retained.

Chapter 4

Towards transpiration cooling applications

4.1 Motivation

In many cases, it is desirable for porous materials to have non-uniform porosity in order to provide performance variation with respect to location on a part. In transpiration cooling, a major design focus has been the optimization of coolant delivery. This means increasing coolant flow at specific locations, while simultaneously reducing it elsewhere. In particular, nose cones and leading edges are considered critical areas on aerospace bodies due to the stagnation point that forms during high-speed flight, leading to increased aero-thermal heating and pressure [5, 62]. An ideal transpiration cooling design for these components will therefore have higher porosity/permeability at such locations in order to deliver more coolant.

With conventional manufacturing methods, it is difficult to intentionally vary the material properties throughout a part. For example, with press-and-sinter powder metallurgy, the porosity of the final product is a function of pressure and temperature, among other variables. These parameters can vary within complex parts during manufacturing, so local porosity may be difficult to predict and control for. Furthermore, the ideal range of porosity for pressed and sintered metals is reported in literature to be between 8 and 20%,

further limiting potential designs. At low porosities, it becomes difficult to prevent full densification, and to ensure the presence of continuous fluid pathways through the material. At higher porosities, the mechanical properties of the structure are too adversely affected; both strength and fatigue resistance suffer [63].

In 2018, Wu et al. conducted experiments on a wedge-shaped nose cone (see Figure 4.1) with a non-uniform porosity: the porosity at the leading edge was increased [64]. They found that this arrangement provided better stagnation point cooling effectiveness compared to a uniform pore geometry, as well as reducing coolant demand. However, because the part was manufactured using traditional pressing and sintering, it had to be constructed using three distinct sections of porous material. This led to large discontinuities in the mass flow rate at the interfaces between the sections (see Figure 4.2).

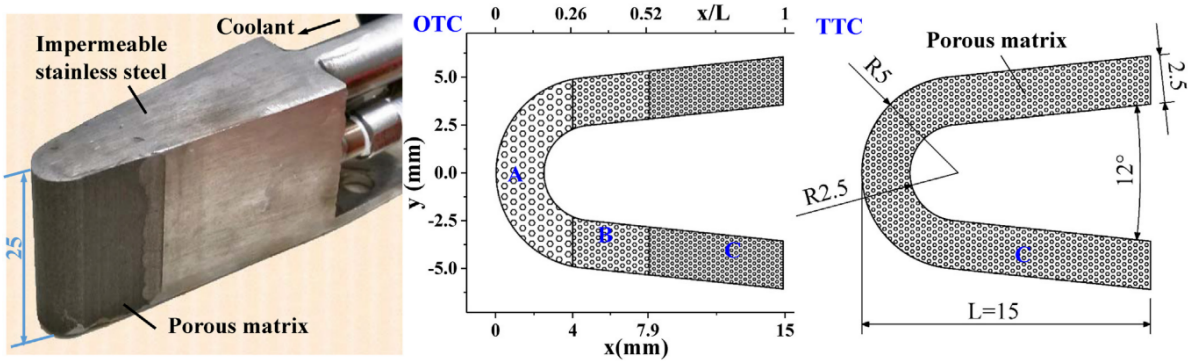

Figure 4.1: Nose cone structure and experimental setup from Wu et al. [64]

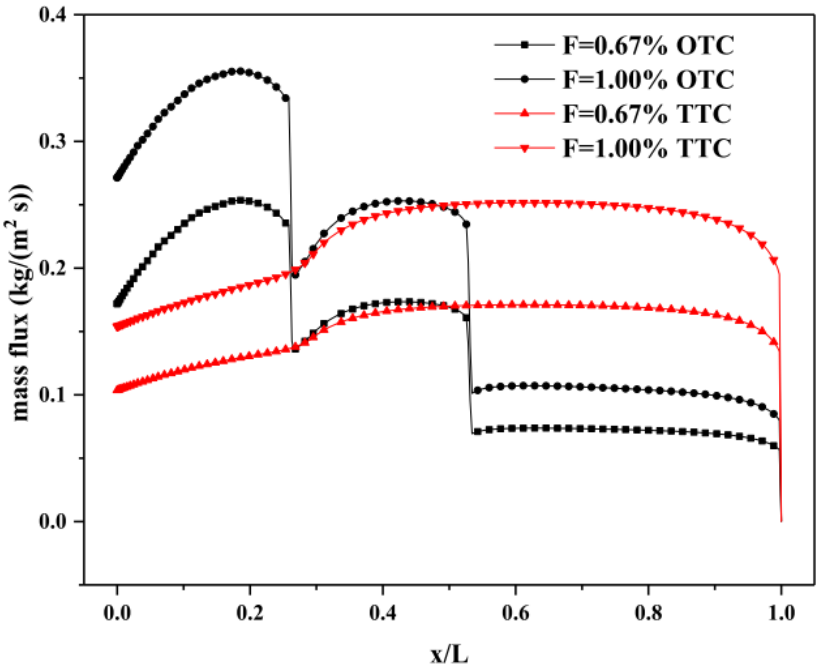

Figure 4.2: Mass flow rate along the outer surface from Wu et al. [64]. The black curves represent the three-part structure at various blowing ratios.

A major advantage of additive manufacturing and TPMS structures is the ease of implementing functional grading: a smooth gradient of volume fraction or other physical properties. Numerous studies have been published on the use of graded TPMS structures, especially for bone tissue engineering [65] and more recently, for controlling flame characteristics in porous media burners [66, 67]. Graded lattice methods have also been shown to be a robust method for improving mechanical strength, especially when combined with topological optimization [68].

The objective of the work in this chapter was therefore to manufacture and simulate a nose cone structure based on the overall geometry from Wu et al., but using functionally-graded TPMS lattices to achieve varying porosity. This was not intended to be a direct performance comparison, but rather the starting point for exploratory work on such complex shapes. Once again, an additional objective was to observe the deviation in performance between design and the as-printed structure. The analysis methods devised in Chapter 3 were applied.

4.2 Methods

4.2.1 Model Generation

The geometry presented in the study by Wu et al. [64] was used as a starting point for the present work. Figure 4.1 shows the dimensions of the overall geometry. Since no experimental work was planned, the overall width (or span) of the structure was decreased from 25 mm to 10 mm, in order to reduce print time and computational complexity.

Two nosecone designs (hereafter termed Designs 1 and 2) incorporating functionally-graded TPMS were created in nTopology (see Figures 4.3 and 4.4). For each design, a gyroid lattice was conformally mapped onto the nosecone geometry. Because of this, the unit cells were not strictly cubic. The basic cell mapping scheme was common to both designs. The thickness of the structure (2.5 mm) was evenly divided into two unit cells. The span was divided into eight unit cells. Eight cell divisions were proportioned along the curved region of the nose cone. Lastly, each straight section was split into 10 unit cells along the streamwise direction, with the specifics differing for the two designs.

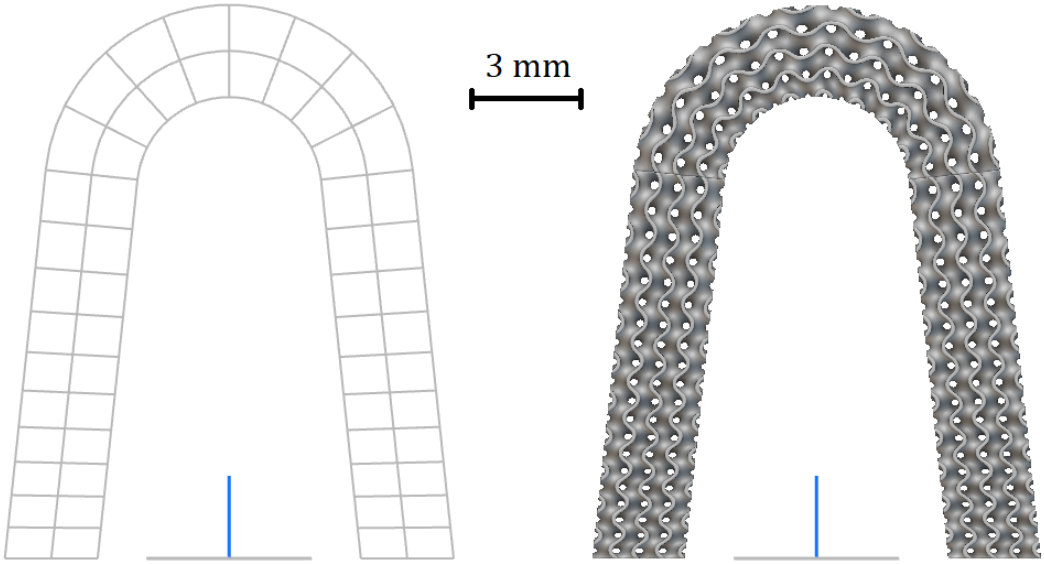

Figure 4.3: Functionally-graded TPMS design 1, with variation in unit cell size.

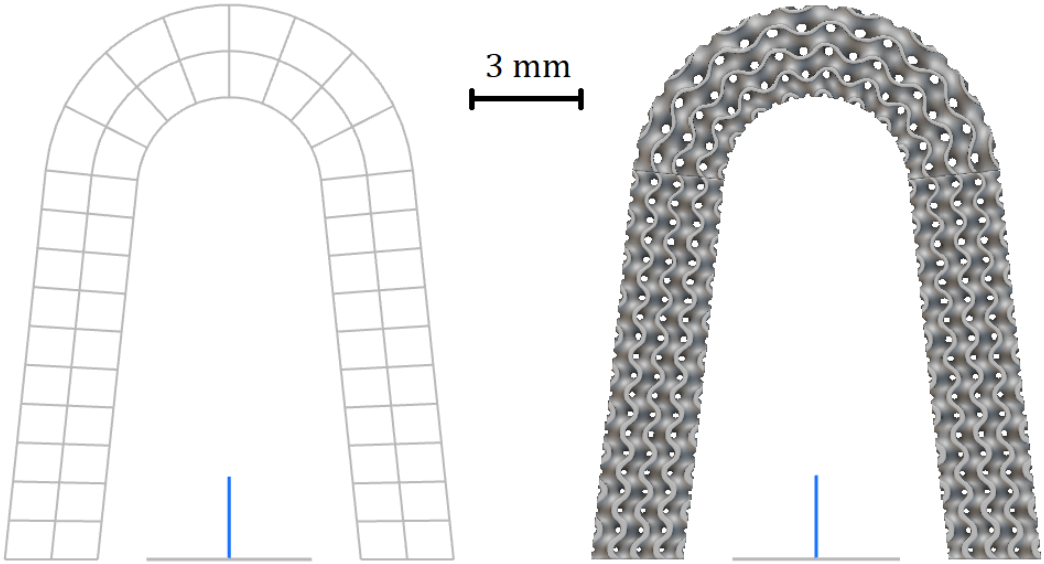

Figure 4.4: Functionally-graded TPMS design 2, with variation in wall thickness.

For Design 1, a ramp function was used to vary the size of these 10 cells, from approximately 1.3 mm to 0.8 mm (moving away from the leading edge). In Design 2, the unit cell size was uniformly maintained at approx. 1 mm, but the wall thickness was increased from 0.15 mm to 0.25 mm. The effect of both these designs was to produce the highest porosity at the leading edge, and decrease it further away.

In addition, a third design was created for the purpose of establishing a baseline case to compare against. This design did not incorporate any functional grading. The unit cell size was maintained at 1 mm and the wall thickness at 0.15 mm. This baseline case was simulated with CFD, but was not fabricated. Table 4.1 provides details for each design.

A deficiency of all three designs was that the TPMS unit cells had to be radially mapped onto the curved section of the leading edge. This led to significant compression of the gyroid structure at the inner radius, and conversely, expansion along the outer radius. Therefore, at the interior of the nosecone, constrictions are formed which limit the flow. It was therefore expected that the flow rate through the leading edge would not necessarily be the highest out of the entire structure. More generally, it was not possible to vary the unit cell size or wall thickness in this curved region without significantly compromising manufacturability. Therefore, the performance in this region for all three designs was

expected to be identical.

Table 4.1: Geometric details of the nosecone designs, with unit cell size in the spanwise direction (z), thickness direction (n), and along the contour in the curved (s_1) and straight (s_2) regions.

Design	Unit cell size [mm]				Wall thickness [mm]	Porosity [%]
	z	n	s_1	s_2		
Design 1	1.25	1.25	0.9 - 1.8	0.8 - 1.3	0.15	76.2
Design 2	1.25	1.25	0.9 - 1.8	1.0	0.15 - 0.25	70.9
Baseline	1.25	1.25	0.9 - 1.8	1.0	0.15	76.1

Due to limitations in latticing and combining of latticed bodies in nTopology, a minor structural discontinuity was present at the joints between the curved and straight sections of the nosecone. In other words, the gyroid lattices did not smoothly merge into each other at these locations. This defect was minor and was not expected to significantly impact the results.

4.2.2 Part Fabrication

Two copies each of Designs 1 and 2 were fabricated via a continuous 400W beam laser powder bed fusion system (EOS M290, EOS GmbH, Krailling, Germany). The material used was maraging steel (BÖHLER Edelstahl GmbH & Co, Austria). The beam focal radius was 50 µm and the layer thickness was 40 µm. Details of the printing process are provided in Table 4.2; parameter optimization and refinement were out of scope from this present work.

Table 4.2: Process parameters for production of the nosecone samples in maraging steel via LPBF.

Parameter Class	Laser Power [W]	Beam Velocity [$\mathrm{m\,s^{-1}}$]	Hatch Distance [µm]	Contour Distance [µm]
Core	335	0.92	100	—
Border	321	0.74		50
Up-skin	225	1	100	—
Down-skin	75	0.5	100	—

4.2.3 Characterization via XCT Scanning

The four printed samples were CT scanned and post-processed using the same method as described in Chapter 3. The voxel size for the scans was 17.5 µm. Due to the major print defects (particularly for Design 2), as well as limitations in scanning capabilities, some of the scan data at the extents of the samples was unusable. This included up to 87 cells (15% of design span) in the z direction, as well as up to 112 cells (13% of design length) at the ends of the straight tail sections (x direction). This meant that identically-sized simulation domains could not be used for all samples, as was the case for the samples in Chapter 3.

4.2.4 LBM Simulation

To analyze the fluid transport characteristics of the nose cone designs, a pressure-driven LBM flow simulation was implemented in Palabos. No freestream flow was considered. An outline of the simulation domain is given in Figure 4.5. A half-symmetry model was used to simplify the computational domain. With two printed samples per design, this allowed four unique simulations for each.

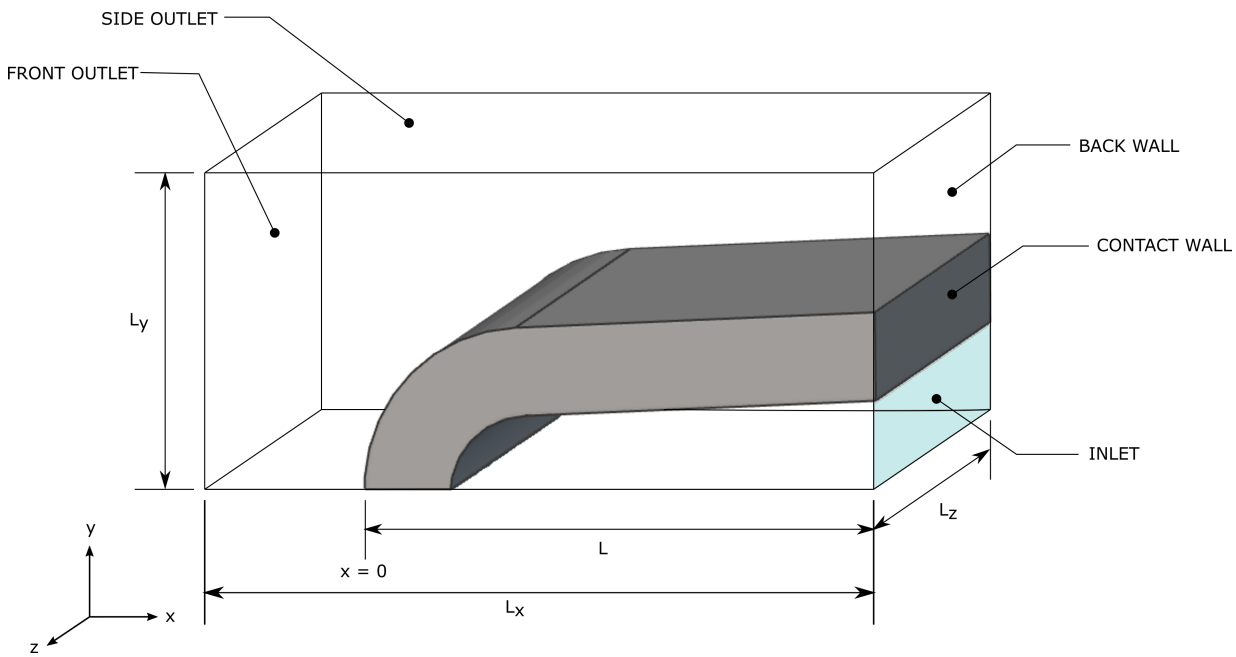

Figure 4.5: Boundary labels and domain characteristics for the nosecone LBM simulations.

The overall simulation domain corresponds to physical dimensions of $L_x = 175\,\text{mm}$, $L_y = 7.9\,\text{mm}$, and L_z ranging from 8.5 to 10 mm. Details of the mesh sizing for each specific case are given in Table 4.3. The flow is driven by a system of pressure boundary conditions. The side outlet and front outlet were set at a uniform pressure value, and a higher pressure is imposed at the inlet, such that the pressure difference was $\Delta P = 1.71 \times 10^{-2}\,\text{Pa}$. The use of pressure boundary conditions at the outlets to approximate a far-field condition is admittedly less than ideal but acceptable since the pressure variation throughout the entire domain is extremely small. Along the plane of symmetry ($y = 0$), a slip wall was prescribed. In LBM, a symmetry boundary condition is functionally identical to a slip wall, and both are implemented by reflecting particle populations specularly, instead of backwards along the incoming direction (as in the bounce-back condition). The "contact wall" was given a no-slip condition, consistent with the experimental setup from Wu et al. [64]. A slip wall was imposed for the region labeled "back wall". During testing, attempts to add a pressure outlet here resulted in spurious behaviour due to the sharp external corner, so the slip wall was used instead.

Table 4.3: Discretization details for each nosecone simulation domain, with the number of cells in each direction and for the structure length L.

Case	N_x	N_L	N_y	N_z	N_{total}
CAD baseline	1000	857	450	571	256 950 000
CAD 1	1000	857	450	571	256 950 000
CAD 2	1000	857	450	571	256 950 000
CT 1-1	1000	855	450	541	243 450 000
CT 1-2	1000	855	450	541	243 450 000
CT 1-3	1000	850	450	541	243 450 000
CT 1-4	1000	850	450	541	243 450 000
CT 2-1	1000	770	450	502	225 900 000
CT 2-2	1000	775	450	502	225 900 000
CT 2-3	1000	745	450	484	217 800 000
CT 2-4	1000	745	450	484	217 800 000

4.3 Results and Discussion

4.3.1 Geometric Analysis

Qualitatively, both Design 1 parts were fabricated to an acceptably high level of fidelity. However, the parts for Design 2 contained significant print defects. In particular, all of the Design 2 samples were visibly underprinted, especially at the leading and trailing edges. A photograph of the printed samples is provided in Figure 4.6. One of the Design 2 samples exhibited a complete collapse of the lattice near the leading edge region (see Figure 4.14), the impacts of which are discussed later.

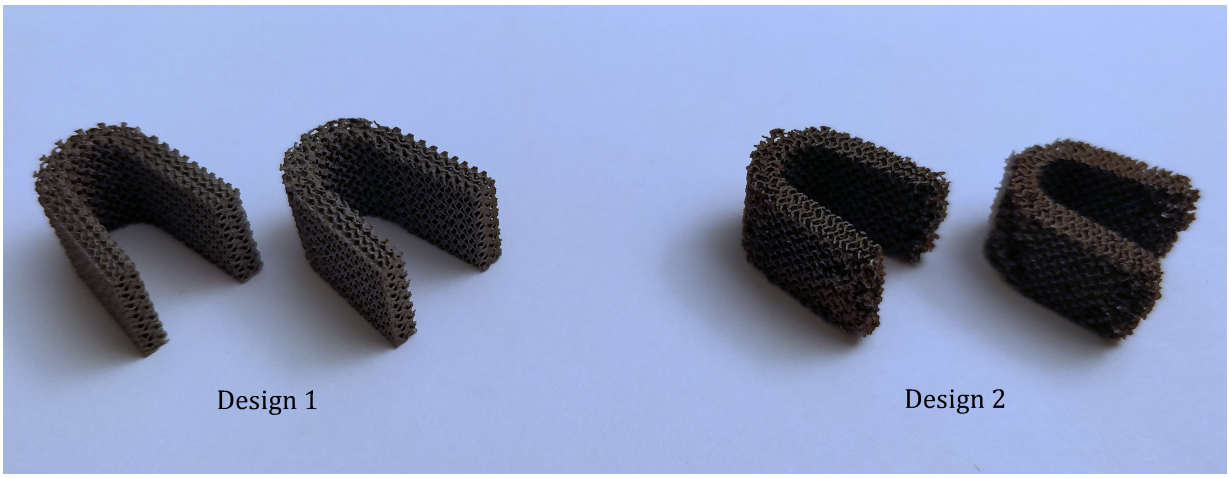

Figure 4.6: Photograph of the printed nosecone designs.

The objective in analyzing print fidelity for the nosecone samples was to assess how well the printed parts followed the design intent of varying porosity. To this end, a new method was devised, which differs from the basic overprint/underprint analysis from section 3.2.4. Each half-structure (as used in the simulation) was subdivided into 15 divisions along the x direction. For each of these divisions, the total number of voxels present was counted, and then divided by the voxel count of the un-latticed volume.

The porosity curves for the three idealized designs are given in Figure 4.7. Unsurprisingly, the CAD geometry behaves exactly as expected. The local porosity for all three is identical for $x/L < 0.3$, since the designs share the same geometry for the curved leading edge. For the baseline case, the porosity is constant in the straight tail section. For Design 1, with the varying unit cell sizes, porosity is higher than the base case closer to the leading edge, and gradually decreases until it is lower. The porosity gradient for Design 2 is even more pronounced, and is entirely lower than baseline.

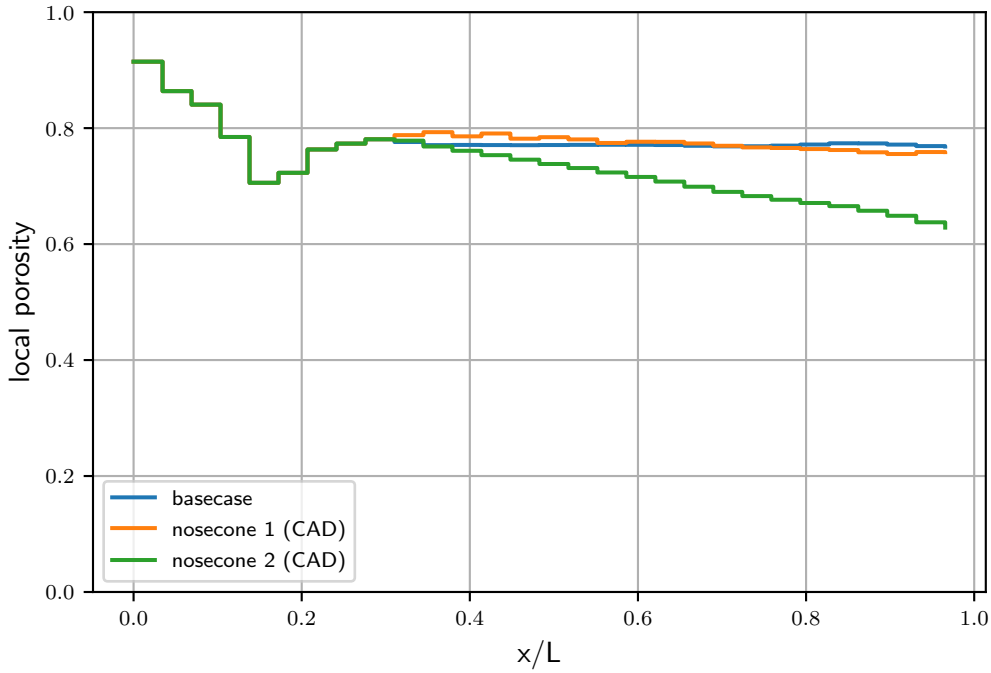

Figure 4.7: Local porosity along the streamwise direction for the design geometries compared to baseline.

The same procedure was then used on the CT scan data to calculate the local porosity of the printed samples. The results are given in Figures 4.8 and 4.9.

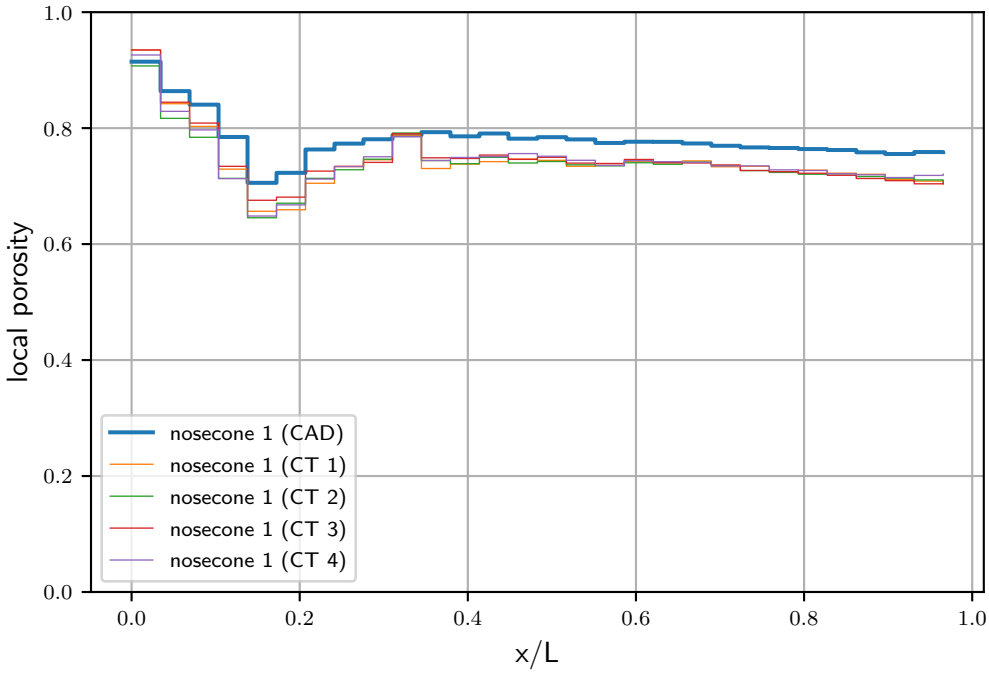

Figure 4.8: Local porosity along the streamwise direction for Design 1.

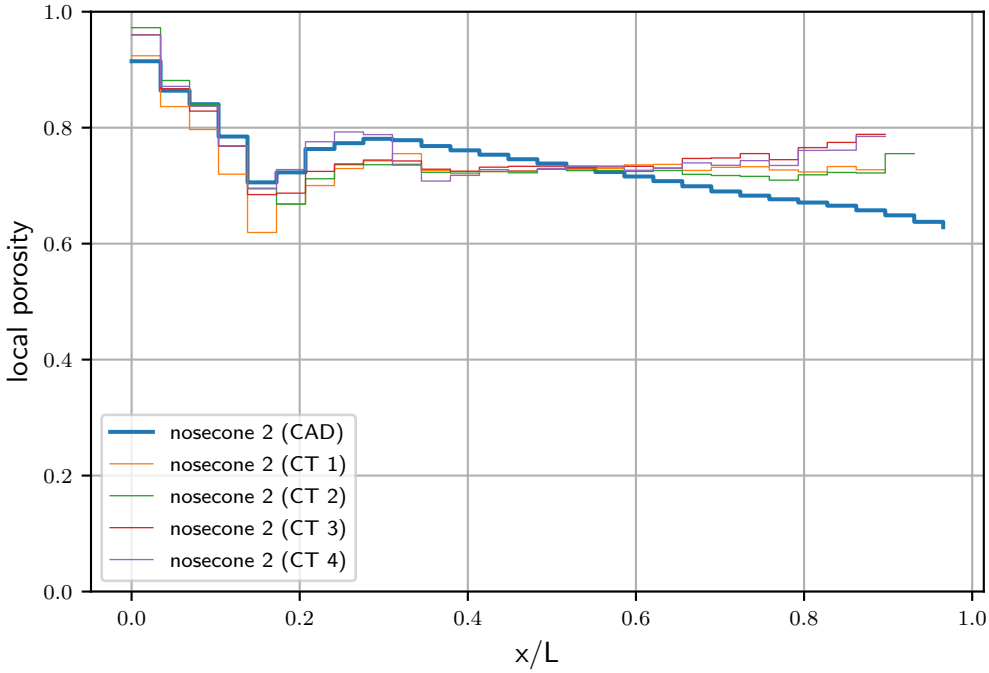

Figure 4.9: Local porosity along the streamwise direction for design 2.

It can clearly be seen that the print fidelity for Design 1 is significantly better than that of Design 2. For Design 1, the local porosity is consistently lower than design, which is indicative of minor overprinting. This is likely due to the inherent inaccuracy of the LPBF process in general, and not because of any major print defects. On the other hand, the as-printed samples for Design 2 completely deviate from the desired geometry. Instead of a decrease in local porosity with increasing x/L, the opposite occurs.

Due to the limited number of printed samples, it is difficult to conclusively state any causes for the print behaviour that was observed. An important factor contributing to the poor print quality at the trailing edges of the samples is the fact that, while TPMS structures are continuous surface lattices, the intersection of the lattice with cutting planes can create unsupported downskin structures which are prone to dross, material vaporization, and significant powder adherence. An example of this in a similar gyroid structure is seen in Figure 4.10. The images illustrate two cutting planes at different parts of the gyroid unit cell, resulting in a defect-free surface in the first case (Subfigure 4.10a), while the other surface (Subfigure 4.10b) has dross-defects due to overhanging downskin features intersecting the cutting plane.

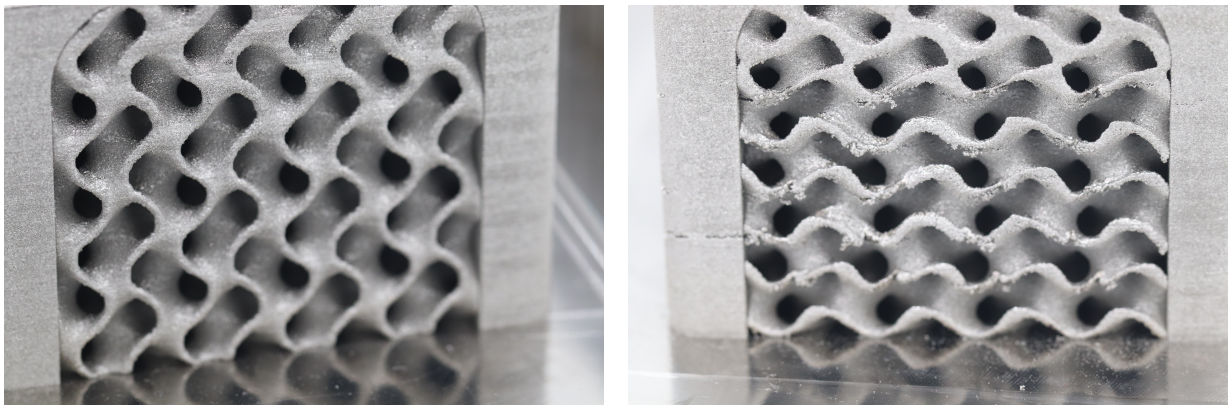

(a) Supported, no defects.

(b) Unsupported, with defects.

Figure 4.10: Two examples of additively-manufactured gyroid structures showing formation of defects due to unsupported geometry at an external cutting plane.

Additionally, based on these few data points, it would seem that the use of varying wall thickness as a method of functional grading produces poorer manufacturability outcomes than the use of varying unit cell size. The very fine structural details did not experience

overprinting and subsequent blockage of the fluid pathways. Instead, these areas were underprinted, often to the point of complete lattice collapse; this is likely due to the discrete number of laser scan lines and challenging scanning strategies for in-filling thin-walled structures. Other factors could have been responsible for this, including incomplete powder spreading, localized material spatter, and localized over-heating due to poor thermal conductivity of surrounding powders. As well, since the two designs were printed in separate print runs, a non-specific problem could have occurred with the second batch such that the print quality was poorer.

4.3.2 Fluid Flow Analysis

Due to the intentionally-varied porosity of the nosecone designs, a single permeability value is neither sufficient nor meaningful for characterizing fluid flow behaviour. Measurement of permeability is further complicated by the curvilinear geometry and varying flow direction.

The primary performance indicator used was the "average exit velocity". This was defined as the flow velocity normal to the local nosecone surface contour, measured as closely as possible to the surface, and averaged along the z direction. For incompressible flow, velocity is directly correlated with mass flow rate, and therefore can provide a good sense of how the flow permeates through the structure. Furthermore, because the pressure boundary conditions were consistent between simulations, the exit velocity can be safely interpreted as an analogue for local permeability.

It was therefore necessary to first identify the outer surface upon which to measure the velocity vectors. For the design geometries, this was straightforward since this contour can be mathematically defined. The equation is piecewise with a circular arc and a straight line:

$$y_{surf} = \begin{cases} \sqrt{r^2 - (x-a)^2} & x/L < \beta \\ mx + y_0 & x/L > \beta \end{cases} \tag{4.1}$$

where β is the transition between the two curves (approx $x/L = 0.3$). Then, the

outward-pointing normal vector for each point on the surface can be obtained, and transformed into a unit normal vector through $\hat{n} = \vec{n}/|\vec{n}|$. The exit velocities are then calculated by taking the dot product of each surface cell's velocity and unit normal vector. These are subsequently averaged over the span, or z direction. Because the printed samples did not perfectly align with the design, it was necessary to map their external surfaces individually. This was done by altering the values of r, m, y_0, and β, by inspection, for each CT simulation case.

To provide a meaningful comparison of the various cases, the exit velocities were normalized by the total average exit velocity for the CAD-only baseline case. Figure 4.11 shows the results for average exit velocity of the idealized designs compared to baseline.

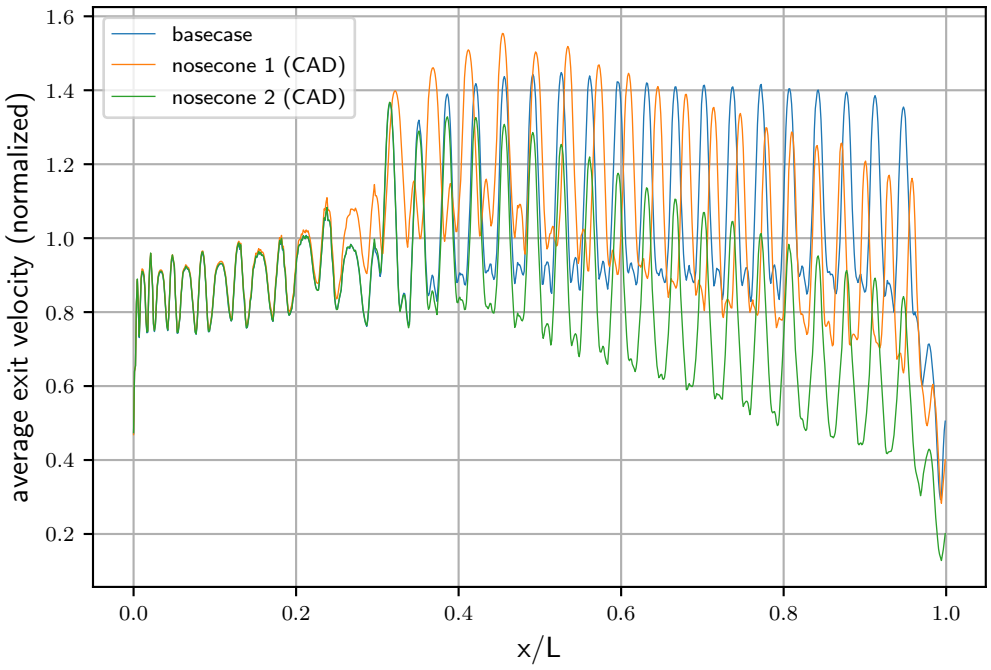

Figure 4.11: Average exit velocity for the design geometries compared to baseline.

The first major observation is that the exit velocities exhibit significant oscillation along the x direction. This is due to the high sampling resolution, which is able to resolve the discrete fluid outlets and non-uniform surface structure. Thus a clear pattern emerges with alternating outlets and "closed-off" regions. These oscillations correspond to the unit cell

size. The baseline case and Design 2 produce oscillations with the same spatial frequency, which is constant throughout the straight tail section. On the other hand, Design 1, which implements a decreasing unit cell size, It is expected that this oscillating behaviour would be smoothed out in the presence of a freestream flow (which was not simulated). However, this does reiterate the general desire in transpiration cooling porous media to reduce the pore size and increase the uniformity of the pore distribution, in order to approach the limits of an ideal homogeneously-permeable structure.

Returning to the simulation results, the behaviour in the curved nose region is identical, as expected, since the geometries there are the same. Moving past this area, the behaviour for each structures differs. The basecase, with no variation in x, maintains a relatively constant exit velocity (ignoring the oscillations). Both functionally-graded designs exhibit a downward trend in velocity towards the trailing edge, thus satisfying the design objective. Design 2, having a slightly lower porosity (refer to Table 4.1), produced an overall lesser bulk flow than Design 1, which also matched expectations.

Each CAD case was then compared against its four corresponding simulations of CT data. These results are given in Figures 4.12 and 4.13.

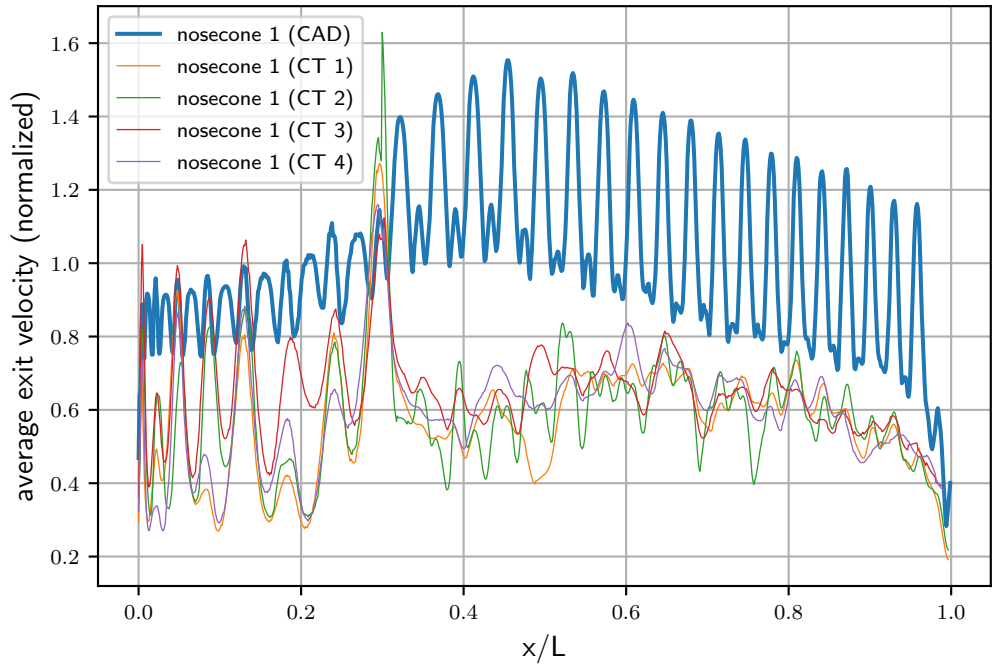

Figure 4.12: Average exit velocity for Design 1. CAD vs CT.

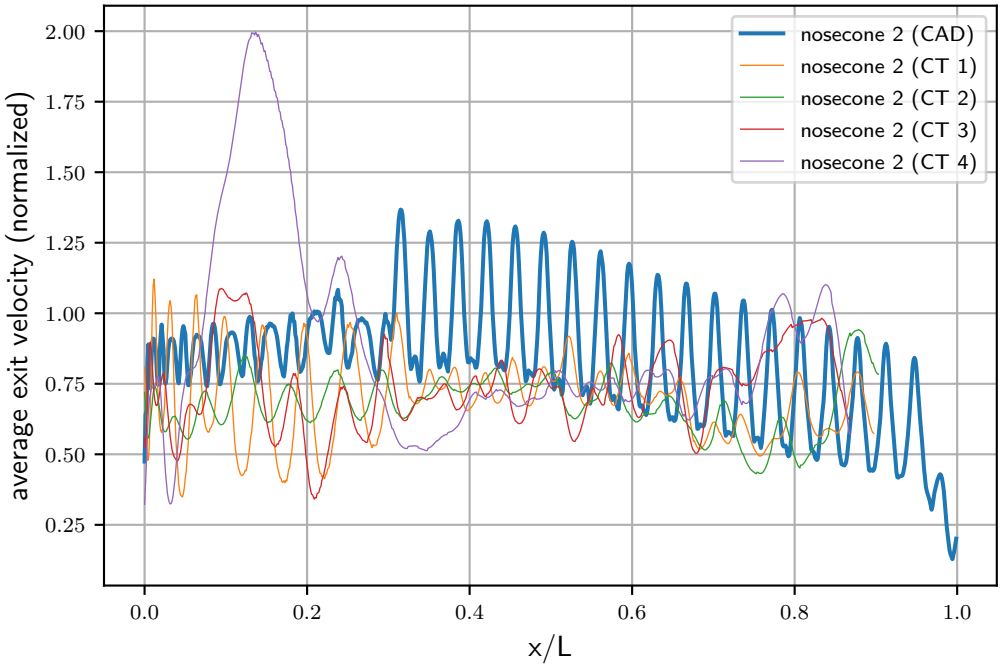

Figure 4.13: Average exit velocity for Design 2. CAD vs CT.

The results for the as-printed cases are striking. In all cases, the average exit velocity is generally lower than for the ideal design, which indicates a lower bulk permeability. This matches the expectations and results from the gyroid disk samples in Chapter 3: increased wall surface area and roughness induce constriction in the flow, reducing peak velocity events. For the CT results, the spatial oscillations in the exit velocity are therefore significantly damped in the straight tails, but strangely are somewhat larger in the leading edge region. This behaviour is difficult to explain, but could be related to the non-constant pore size due to the conformal mapping of the lattice. Any misprinting, particularly at the inner radius where flow throttling occurs, could have greatly amplified effects of either increasing or decreasing flow permeability.

For Design 2, the reversal observed in the porosity gradient in Figure 4.9 manifests as a corresponding reversal in the average exit velocity. Indeed, it can be seen that cases CT 3 and CT 4 (two halves of the same part), which experienced the most underprinting at the trailing edge, produce the highest average exit velocity at that region. Another major observation can be made for Design 2, case CT 4, which contained a large misprinted region around $x/L = 0.15$ (see Figure 4.14. The average exit velocity for that case peaks significantly, showing that millimeter-scale defects in such parts can cause vastly unforeseen behaviour.

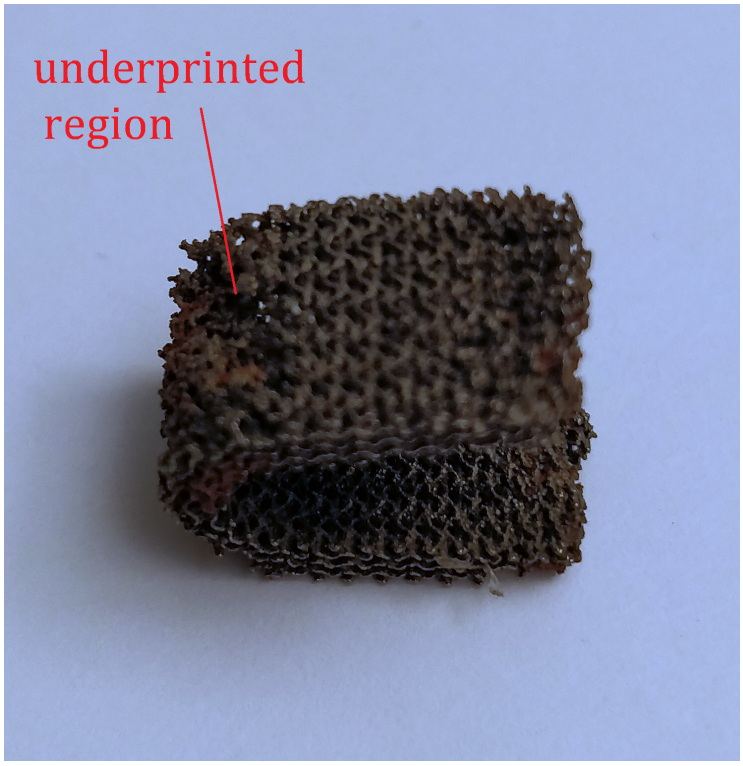

Figure 4.14: Photo of the second Design 2 printed part, showing the underprinted region of lattice collapse.

Next, an integral measure was calculated to gain a better understanding of the total flow rate for each case. A summation of the average exit velocity data was taken along z, and the cumulative sum plotted along x/L. To provide a consistent comparison, only the region in x common to all datasets was studied (i.e. the data past $x/L > 0.87$ was truncated). As well, each dataset was normalized by the number of cells in z, to account for the different spanwise sizes of the simulation domains. The final cumulative sum of velocity for the baseline case was set to unity, and all other cases are benchmarked against it. The y-axis value at any given point on a curve is therefore a measure of the total amount of fluid leaving the surface, from the leading edge, up to that x/L location. The results of this analysis are given in Figures 4.15 and 4.16.

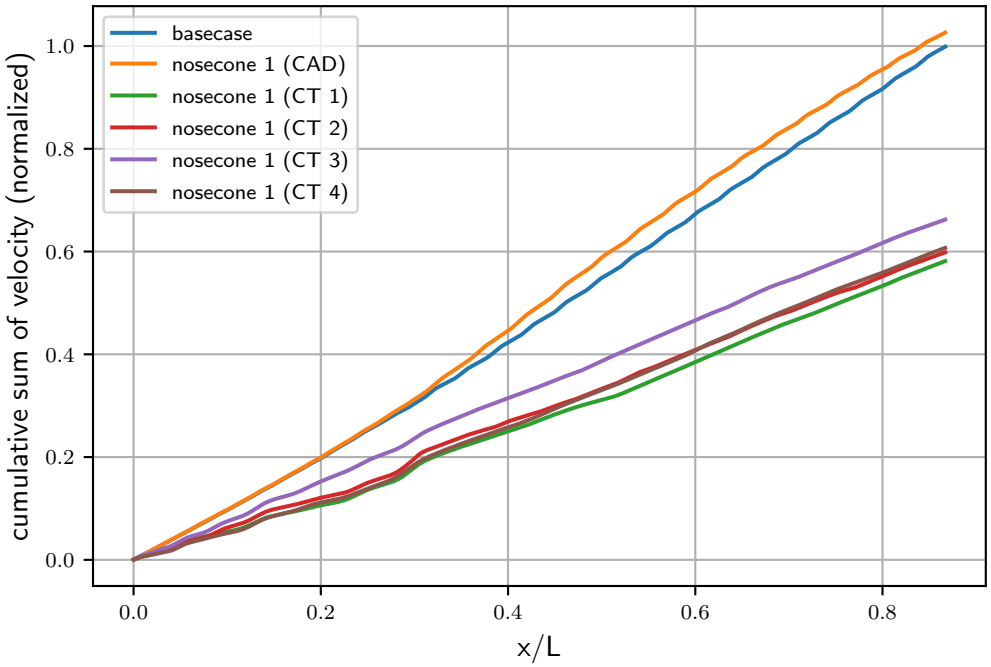

Figure 4.15: Normalized exit velocity integral for Design 1. CAD vs CT.

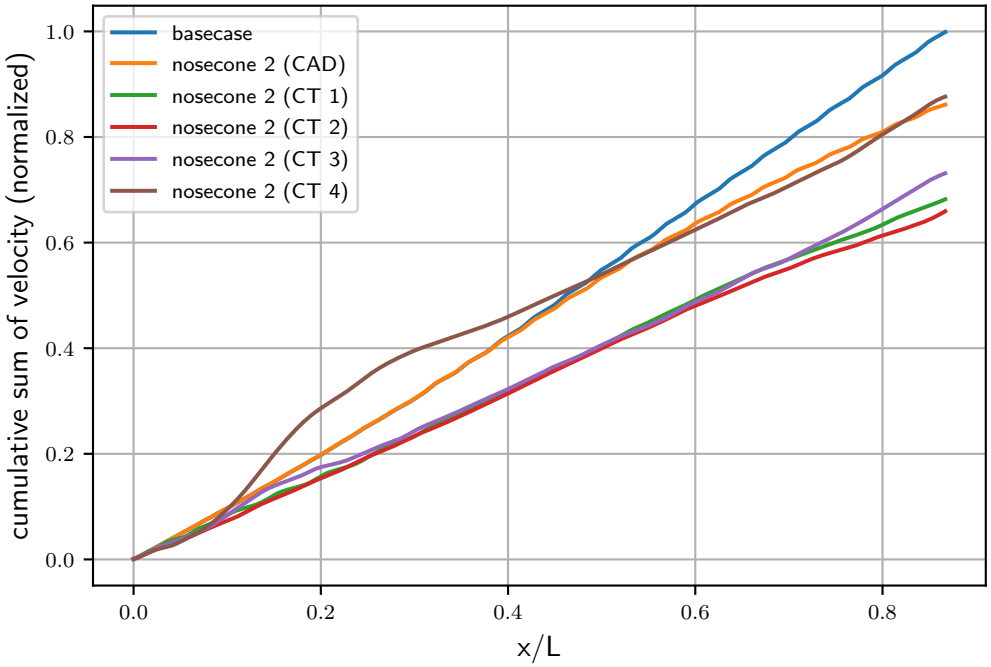

Figure 4.16: Normalized exit velocity integral for Design 2. CAD vs CT.

From these figures, the magnitude of the difference in total flow can be readily observed. Beginning with the design geometries, Design 2 produces a modest 14% decrease in total flow compared to baseline, and Design 1 actually increases total flow by 2%. These values track well with the trends in local porosity and average exit velocity. The real story, however, is told by the as-printed geometry. Compared to their respective CAD geometries, the Design 1 prints show an approximate 41% decrease in total flow, and the Design 2 prints deviate by about 20%. Only Design 2 case CT 4 produces a similar total flow as the ideal geometry, and this is solely due to the large misprinted void near the leading edge, which produces a large spike in the velocity integral.

Contrasted to the disk samples in Chapter 3, which exhibited a maximum of 14.8% deviation in permeability (and therefore bulk flow rate) between CAD and CT, the performance difference for the nosecone parts is much more aggressive. This does seem to support the hypothesis that designs with smaller unit cell sizes are more susceptible to the real effects of the print process, and thus deviate more from their intended design behaviour.

Chapter 5

Conclusions

The methodology outlined in this work provides a systematic approach to quantify both the geometric fidelity of printed TPMS architecture and the theoretical fluidic properties of the flow. The voxel-based approach was geometry-agnostic, allowing very fine discretization of both the original design and the as-printed geometry, without the need for bulky triangular meshes. This is a key advantage when working with highly-complex geometry. Both the CFD simulation and the geometric analysis are able to use this format of 3D representation. Lattice Boltzmann method CFD simulation is well suited to model the fluid flow behaviour through complex TPMS geometry. In particular, it was capable of handling the highly complex wall boundaries involved for the as-printed part, which would not be possible with more conventional CFD approaches.

The comparison of ideal and as-printed TPMS geometry enabled a meaningful quantification of the bulk flow properties. Although in many cases the overall porosity of the printed part closely matched the original design, non-negligible over- and underprinting occurred during fabrication, which could be analyzed on a more localized basis, either layer-by-layer or in discrete regions. The simulated permeability of the as-printed structure was consistently lower than that of its CAD model, owing to the irregular surface topography which imposed a greater wall surface area. Correspondingly, for the same pressure drop imposed across both geometries, the bulk velocity through the as-printed structure was lower. Particularly for the functionally-graded nosecone designs, the difference was

significant and would almost certainly impact the real performance of such structures.

The attempt at classifying the design space met with limited success. The simulations were able to show a clear relationship between porosity, or more accurately, pore size, and fluid permeability. Direct control over the structural properties is facilitated by the variables of unit cell size and wall thickness in a TPMS, which can be smoothly varied across a volume. The results of this research naturally invite the investigation of more lattice structures such as the remaining TPMS types and other porous geometries. Quantifying the effect of as-printed part morphology across different TPMS sizes was less conclusive. There was no clear trend for how the print inaccuracies manifested with respect to differing structure sizes.

The outcome of this research will be valuable in streamlining the design of these structures to meet desired fluid flow and heat transfer performance requirements. This could potentially include the use of functional grading to produce non-uniform cooling, and topology optimization to solve the inverse design problem. Besides the aerospace applications, developments in the understanding of fluid flow through TPMS structures will also have direct benefits for biomedical, thermal, and chemical engineering. Opportunities for further research in this area could focus on providing more insight into the physics of the fluid flow phenomena, in order to better reconcile numerical simulations with experiment. This includes endeavours such as examining wall shear stress, heat transfer, and extending the analysis into the inertial (Forchheimer) regime (with consequential turbulence effects).

References

[1] M. Arai and T. Suidzu, "Porous ceramic coating for transpiration cooling of gas turbine blade," *Journal of Thermal Spray Technology*, vol. 22, no. 5, pp. 690–698, 2013.

[2] M. Kuhn and H. Hald, "Application of Transpiration Cooling for Hot Structures," in *RESPACE – Key Technologies for Reusable Space Systems*, vol. 98, pp. 82–103, Berlin, Heidelberg: Springer Berlin Heidelberg, 2008.

[3] A. O. Aremu, I. Maskery, C. Tuck, I. A. Ashcroft, R. D. Wildman, and R. I. Hague, "A comparative finite element study of cubic unit cells for selective laser melting," in *25th Annual International Solid Freeform Fabrication Symposium &#65533; An Additive Manufacturing Conference, SFF 2014*, pp. 1238–1249, 2014.

[4] J. Kelley and L'Ecuyer M.R., "Transpiration Cooling, Its Theory and Application," *NASA CR-76367*, 1966.

[5] H. Bohrk, "Transpiration-Cooling with Porous Ceramic Composites in Hypersonic Flow," in *Porous media in high temperature and high speed flows*, NATO, 2016.

[6] T. Hayashi, "Transpiration cooling structure effects on the strength of 3D-woven SiC/SiC composites under thermal cycling," *Ceramic Engineering and Science Proceedings*, vol. 26, no. 2, pp. 335–342, 2005.

[7] L. Shen, J. Wang, W. Dong, J. Pu, J. Peng, D. Qu, and L. Chen, "An experimental investigation on transpiration cooling with phase change under supersonic condition," *Applied Thermal Engineering*, vol. 105, pp. 549–556, 2016.

[8] W. Dahmen, T. Gotzen, S. Müller, and M. Rom, "Numerical simulation of transpiration cooling through porous material," *International Journal for Numerical Methods in Fluids*, 2014.

[9] D. Greuel, A. Herbertz, O. J. Haidn, M. Ortelt, and H. Hald, "Transpiration cooling applied to C/C liners of cryogenic liquid rocket engines," in *40th AIAA/ASME/SAE/ASEE Joint Propulsion Conference and Exhibit*, (Reston, Virigina), American Institute of Aeronautics and Astronautics, July 2004.

[10] N. Christopher, J. M. Peter, M. J. Kloker, and J. P. Hickey, "DNS of turbulent flat-plate flow with transpiration cooling," *International Journal of Heat and Mass Transfer*, vol. 157, p. 119972, 2020.

[11] R. Krewinkel, "A review of gas turbine effusion cooling studies," *International Journal of Heat and Mass Transfer*, vol. 66, pp. 706–722, 2013.

[12] P. K. Gokuldoss, S. Kolla, and J. Eckert, "Additive manufacturing processes: Selective laser melting, electron beam melting and binder jetting-selection guidelines," *Materials*, vol. 10, no. 6, 2017.

[13] S. Sun, M. Brandt, and M. Easton, *Powder bed fusion processes: An overview*. Elsevier Ltd, 2017.

[14] W. E. King, A. T. Anderson, R. M. Ferencz, N. E. Hodge, C. Kamath, S. A. Khairallah, and A. M. Rubenchik, "Laser powder bed fusion additive manufacturing of metals; physics, computational, and materials challenges," *Applied Physics Reviews*, vol. 2, no. 4, p. 041304, 2015.

[15] K. Moussaoui, W. Rubio, M. Mousseigne, T. Sultan, and F. Rezai, "Effects of Selective Laser Melting additive manufacturing parameters of Inconel 718 on porosity, microstructure and mechanical properties," *Materials Science and Engineering A*, vol. 735, no. April, pp. 182–190, 2018.

[16] M. W. Wu, J. K. Chen, B. H. Lin, and P. H. Chiang, "Improved fatigue endurance ratio of additive manufactured Ti-6Al-4V lattice by hot isostatic pressing," *Materials and Design*, vol. 134, pp. 163–170, 2017.

[17] M. Ziaee and N. B. Crane, "Binder jetting: A review of process, materials, and methods," *Additive Manufacturing*, vol. 28, no. December 2018, pp. 781–801, 2019.

[18] S. Patel, A. Rogalsky, and M. Vlasea, "Towards understanding side-skin surface characteristics in laser powder bed fusion," *Journal of Materials Research*, vol. 35, no. 15, pp. 2055–2064, 2020.

[19] D. Dickstein, D. Donghyun Ko, W. Nadvornick, K. Jain, S. Holdheim, Y. Sungtaek Ju, and N. Ghoniem, "Optimized Permeability of Microporous Foam for Transpiration Cooling in Hypersonic Leading Edge," *Journal of Thermophysics and Heat Transfer*, pp. 1–13, 2022.

[20] I. Maskery, L. Sturm, A. O. Aremu, A. Panesar, C. B. Williams, C. J. Tuck, R. D. Wildman, I. A. Ashcroft, and R. J. Hague, "Insights into the mechanical properties of several triply periodic minimal surface lattice structures made by polymer additive manufacturing," *Polymer*, vol. 152, pp. 62–71, 2018.

[21] L. Han and S. Che, "An Overview of Materials with Triply Periodic Minimal Surfaces and Related Geometry: From Biological Structures to Self-Assembled Systems," *Advanced Materials*, vol. 30, no. 17, pp. 1–22, 2018.

[22] C. Yan, L. Hao, A. Hussein, and P. Young, "Ti-6Al-4V triply periodic minimal surface structures for bone implants fabricated via selective laser melting," *Journal of the Mechanical Behavior of Biomedical Materials*, vol. 51, pp. 61–73, 2015.

[23] J. Feng, J. Fu, X. Yao, and Y. He, "Triply periodic minimal surface (TPMS) porous structures: from multi-scale design, precise additive manufacturing to multidisciplinary applications," *International Journal of Extreme Manufacturing*, vol. 4, no. 2, p. 022001, 2022.

[24] B. Zhang, J. Huang, W. Li, H. Huang, H. Zhao, and J. Peng, "Synthesis and characterization of light-weight porous ceramics used in the transpiration cooling," *Acta Astronautica*, vol. 177, no. June, pp. 438–445, 2020.

[25] L. Yang, C. Yan, C. Han, P. Chen, S. Yang, and Y. Shi, "Mechanical response of a triply periodic minimal surface cellular structures manufactured by selective laser melting," *International Journal of Mechanical Sciences*, vol. 148, no. August, pp. 149–157, 2018.

[26] K. Wei, J. Wang, and M. Mao, "Model Discussion of Transpiration Cooling with Boiling," *Transport in Porous Media*, vol. 94, no. 1, pp. 303–318, 2012.

[27] A. Van Foreest, M. Sippel, A. Gülhan, B. Esser, B. A. Ambrosius, and K. Sudmeijer, "Transpiration cooling using liquid water," *Journal of Thermophysics and Heat Transfer*, vol. 23, no. 4, pp. 693–702, 2009.

[28] D. Prokein and J. von Wolfersdorf, "Numerical simulation of turbulent boundary layers with foreign gas transpiration using OpenFOAM," *Acta Astronautica*, vol. 158, no. March, pp. 253–263, 2019.

[29] P. Jiang, Z. Liao, Z. Huang, Y. Xiong, and Y. Zhu, "Influence of shock waves on supersonic transpiration cooling," *International Journal of Heat and Mass Transfer*, vol. 129, pp. 965–974, 2019.

[30] Y. Sudhakar, U. Lācis, S. Pasche, and S. Bagheri, "Higher-Order Homogenized Boundary Conditions for Flows Over Rough and Porous Surfaces," *Transport in Porous Media*, vol. 136, no. 1, pp. 1–42, 2021.

[31] G. Łukaszewicz and P. Kalita, *Navier–Stokes Equations*. Advances in Mechanics and Mathematics, Cham: Springer International Publishing, 9 2016.

[32] T. Kruger, H. Kusumaatmaja, A. Kuzmin, O. Shardt, S. Goncalo, and E. M. Viggen, *The lattice boltzmann method, principles and practice*, vol. 10. 2017.

[33] M. A. Gallivan, D. R. Noble, J. G. Georgiadis, and R. O. Buckius, "An evaluation of the bounce-back boundary condition for lattice Boltzmann simulations," *International Journal for Numerical Methods in Fluids*, vol. 25, no. 3, pp. 249–263, 1997.

[34] D. Ali, M. Ozalp, S. B. Blanquer, and S. Onel, "Permeability and fluid flow-induced wall shear stress in bone scaffolds with TPMS and lattice architectures: A CFD analysis," *European Journal of Mechanics, B/Fluids*, vol. 79, pp. 376–385, 2020.

[35] Z. Cheng, X. Li, R. Xu, and P. Jiang, "Investigations on porous media customized by triply periodic minimal surface: Heat transfer correlations and strength performance," *International Communications in Heat and Mass Transfer*, vol. 129, p. 105713, 2021.

[36] T. Pires, J. Santos, R. B. Ruben, B. P. Gouveia, A. P. Castro, and P. R. Fernandes, "Numerical-experimental analysis of the permeability-porosity relationship in triply periodic minimal surfaces scaffolds," *Journal of Biomechanics*, vol. 117, p. 110263, 2021.

[37] M. Safdari Shadloo, "Numerical simulation of compressible flows by lattice Boltzmann method," *Numerical Heat Transfer; Part A: Applications*, vol. 75, no. 3, pp. 167–182, 2019.

[38] K. V. Sharma, R. Straka, and F. W. Tavares, "Current status of Lattice Boltzmann Methods applied to aerodynamic, aeroacoustic, and thermal flows," *Progress in Aerospace Sciences*, vol. 115, no. March, p. 100616, 2020.

[39] J. Santos, T. Pires, B. P. Gouveia, A. P. Castro, and P. R. Fernandes, "On the permeability of TPMS scaffolds," *Journal of the Mechanical Behavior of Biomedical Materials*, vol. 110, no. June, pp. 1–7, 2020.

[40] I. Echeta, X. Feng, B. Dutton, R. Leach, and S. Piano, "Review of defects in lattice structures manufactured by powder bed fusion," *International Journal of Advanced Manufacturing Technology*, vol. 106, no. 5-6, pp. 2649–2668, 2020.

[41] I. Kaur and P. Singh, "Flow and thermal transport characteristics of Triply-Periodic Minimal Surface (TPMS)-based gyroid and Schwarz-P cellular materials," *Numerical Heat Transfer; Part A: Applications*, vol. 79, no. 8, pp. 553–569, 2021.

[42] D. A. Clarke, F. Dolamore, C. J. Fee, P. Galvosas, and D. J. Holland, "Investigation of flow through triply periodic minimal surface-structured porous media using MRI and CFD," *Chemical Engineering Science*, no. xxxx, p. 116264, 2020.

[43] Y. Jung and S. Torquato, "Fluid permeabilities of triply periodic minimal surfaces," *Physical Review E - Statistical, Nonlinear, and Soft Matter Physics*, vol. 72, no. 5, pp. 1–8, 2005.

[44] M. Leary, M. Mazur, H. Williams, E. Yang, A. Alghamdi, B. Lozanovski, X. Zhang, D. Shidid, L. Farahbod-Sternahl, G. Witt, I. Kelbassa, P. Choong, M. Qian, and M. Brandt, "Inconel 625 lattice structures manufactured by selective laser melting (SLM): Mechanical properties, deformation and failure modes," *Materials and Design*, vol. 157, no. 2017, pp. 179–199, 2018.

[45] T. Maconachie, M. Leary, B. Lozanovski, X. Zhang, M. Qian, O. Faruque, and M. Brandt, "SLM lattice structures: Properties, performance, applications and challenges," *Materials and Design*, vol. 183, p. 108137, 2019.

[46] C. Pauzon, T. Mishurova, M. Fischer, J. Ahlström, T. Fritsch, G. Bruno, and E. Hryha, "Impact of contour scanning and helium-rich process gas on performances of Alloy 718 lattices produced by laser powder bed fusion," *Materials and Design*, vol. 215, p. 110501, 2022.

[47] H. Soni, M. Gor, G. Singh Rajput, and P. Sahlot, "A comprehensive review on effect of process parameters and heat treatment on tensile strength of additively manufactured Inconel-625," *Materials Today: Proceedings*, vol. 47, pp. 4866–4871, 2021.

[48] K. D. Ramkumar, W. S. Abraham, V. Viyash, N. Arivazhagan, and A. M. Rabel, "Investigations on the microstructure, tensile strength and high temperature corrosion

behaviour of Inconel 625 and Inconel 718 dissimilar joints," *Journal of Manufacturing Processes*, vol. 25, pp. 306–322, 2017.

[49] Z. Min, G. Huang, S. N. Parbat, L. Yang, and M. K. Chyu, "Experimental investigation on additively manufactured transpiration and film cooling structures," *Journal of Turbomachinery*, vol. 141, no. 3, 2019.

[50] N. Otsu, "A Threshold Selection Method from Gray-Level Histograms," *IEEE Transactions on Systems, Man, and Cybernetics*, vol. 9, pp. 62–66, 1 1979.

[51] M. Dallago, S. Raghavendra, V. Luchin, G. Zappini, D. Pasini, and M. Benedetti, "Geometric assessment of lattice materials built via Selective Laser Melting," *Materials Today: Proceedings*, vol. 7, pp. 353–361, 2019.

[52] H. Wang, P. Chen, H. Wu, A. Chen, S. Wu, J. Su, M. Wang, X. Feng, C. Yang, L. Yang, C. Yan, and Y. Shi, "Comparative evaluation of printability and compression properties of poly-ether-ether-ketone triply periodic minimal surface scaffolds fabricated by laser powder bed fusion," *Additive Manufacturing*, vol. 57, no. May, p. 102961, 2022.

[53] J. Latt, O. Malaspinas, D. Kontaxakis, A. Parmigiani, D. Lagrava, F. Brogi, M. B. Belgacem, Y. Thorimbert, S. Leclaire, S. Li, F. Marson, J. Lemus, C. Kotsalos, R. Conradin, C. Coreixas, R. Petkantchin, F. Raynaud, J. Beny, and B. Chopard, "Palabos: Parallel Lattice Boltzmann Solver," *Computers and Mathematics with Applications*, vol. 81, pp. 334–350, 2021.

[54] S. K. Kang and Y. A. Hassan, "The effect of lattice models within the lattice Boltzmann method in the simulation of wall-bounded turbulent flows," *Journal of Computational Physics*, vol. 232, no. 1, pp. 100–117, 2013.

[55] R. Mei, W. Shyy, D. Yu, and L. S. Luo, "Lattice Boltzmann Method for 3-D Flows with Curved Boundary," *Journal of Computational Physics*, vol. 161, no. 2, pp. 680–699, 2000.

[56] A. El Elmi, D. Melancon, M. Asgari, L. Liu, and D. Pasini, "Experimental and numerical investigation of selective laser melting-induced defects in Ti-6Al-4V octet truss

lattice material: The role of material microstructure and morphological variations," *Journal of Materials Research*, vol. 35, no. 15, pp. 1900–1912, 2020.

[57] E. Hernández-Nava, S. Tammas-Williams, C. Smith, F. Leonard, P. J. Withers, I. Todd, and R. Goodall, "X-ray tomography characterisation of lattice structures processed by Selective Electron Beam Melting," *Metals*, vol. 7, no. 8, 2017.

[58] N. Soro, N. Saintier, H. Attar, and M. S. Dargusch, "Surface and morphological modification of selectively laser melted titanium lattices using a chemical post treatment," *Surface and Coatings Technology*, vol. 393, no. December 2019, p. 125794, 2020.

[59] Y. Hu, D. Li, S. Shu, and X. Niu, "Simulation of steady fluid-solid conjugate heat transfer problems via immersed boundary-lattice Boltzmann method," *Computers and Mathematics with Applications*, vol. 70, no. 9, pp. 2227–2237, 2015.

[60] F. M. White, *Fluid Mechanics*. New York: McGraw-Hill Education, 8 ed., 2017.

[61] A. A. Zick and G. M. Homsy, "Stokes flow through periodic arrays of spheres," *Journal of Fluid Mechanics*, vol. 115, p. 13, 2 1982.

[62] T. Reimer, M. Kuhn, A. Gülhan, B. Esser, M. Sippel, and A. V. Foreest, "Transpiration cooling tests of porous cmc in hypersonic flow," *17th AIAA International Space Planes and Hypersonic Systems and Technologies Conference 2011*, no. April, pp. 1–13, 2011.

[63] H. Yuan, L. Zhang, and S. Ma, "Damage evolution and characterization for sintered powder metals with the varying porosity," *Engineering Fracture Mechanics*, vol. 207, pp. 86–98, 2019.

[64] N. Wu, J. Wang, F. He, L. Chen, and B. Ai, "Optimization transpiration cooling of nose cone with non-uniform permeability," *International Journal of Heat and Mass Transfer*, vol. 127, pp. 882–891, 2018.

[65] J. Maszybrocka, B. Gapinski, M. Dworak, G. Skrabalak, and A. Stwora, "Modelling, manufacturability and compression properties of the cpti grade 2 cellular lattice with

radial gradient tpms architecture," *Bulletin of the Polish Academy of Sciences: Technical Sciences*, vol. 67, no. 4, pp. 719–727, 2019.

[66] S. Sobhani, S. Allan, P. Muhunthan, E. Boigne, and M. Ihme, "Additive Manufacturing of Tailored Macroporous Ceramic Structures for High-Temperature Applications," *Advanced Engineering Materials*, vol. 22, no. 8, pp. 1–8, 2020.

[67] S. Sobhani, P. Muhunthan, E. Boigné, D. Mohaddes, and M. Ihme, "Experimental feasibility of tailored porous media burners enabled via additive manufacturing," *Proceedings of the Combustion Institute*, vol. 000, pp. 1–10, 2020.

[68] A. Panesar, M. Abdi, D. Hickman, and I. Ashcroft, "Strategies for functionally graded lattice structures derived using topology optimisation for Additive Manufacturing," *Additive Manufacturing*, vol. 19, pp. 81–94, 2018.

APPENDICES

A Gyroid Disks: Geometric Analysis Results

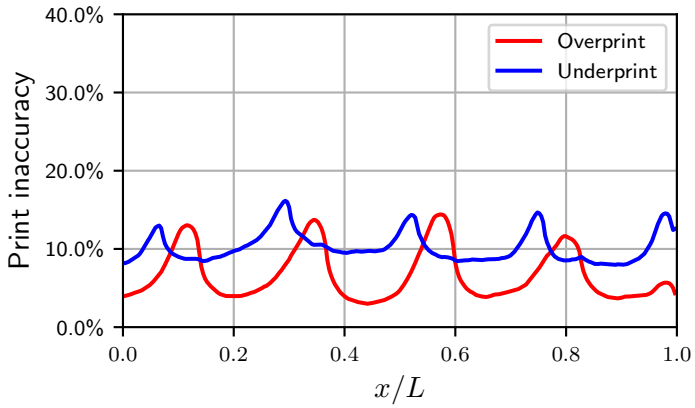

Figure 1: Measures of print geometric deviation calculated on a layer-by-layer basis for Design 2.

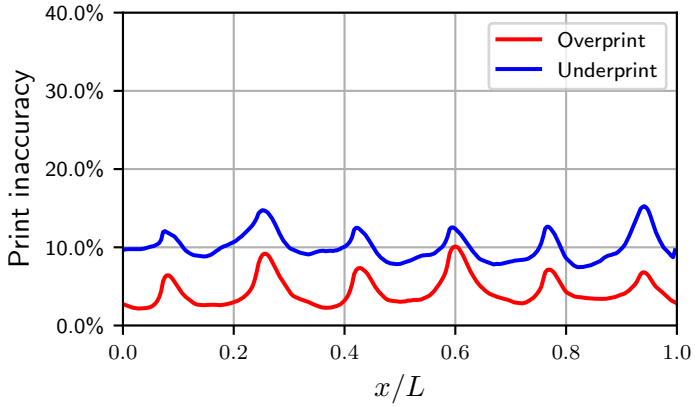

Figure 2: Measures of print geometric deviation calculated on a layer-by-layer basis for Design 3.

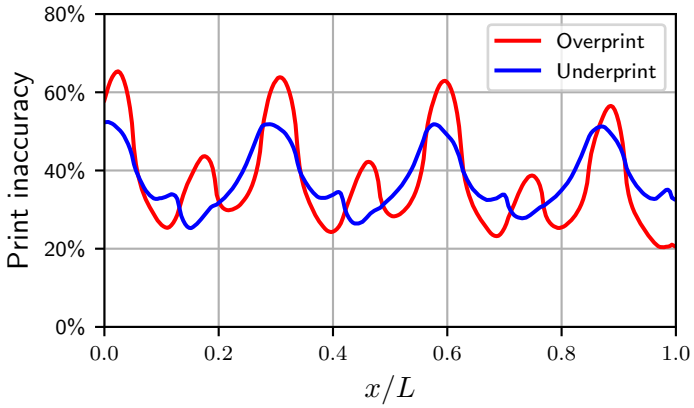

Figure 3: Measures of print geometric deviation calculated on a layer-by-layer basis for Design 4.

B Gyroid Disks: Complete Fluid Flow Analysis Results

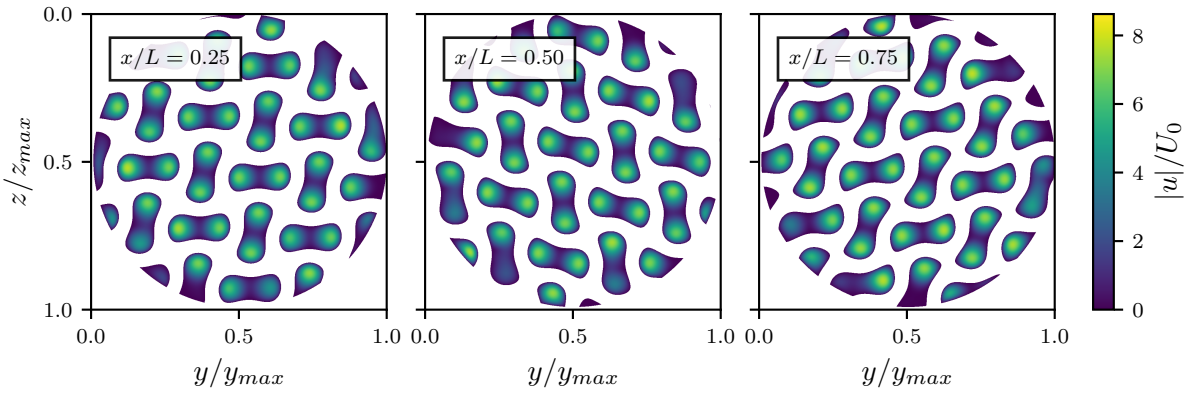

Figure 4: Velocity magnitude profiles at three cross-sectional locations for the CAD data of Design 2.

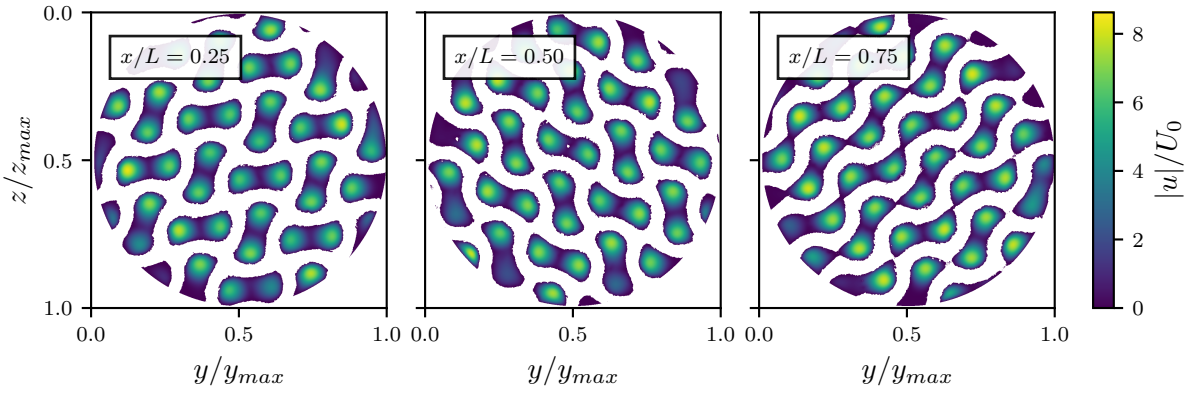

Figure 5: Velocity magnitude profiles at three cross-sectional locations for the CT data of Design 2.

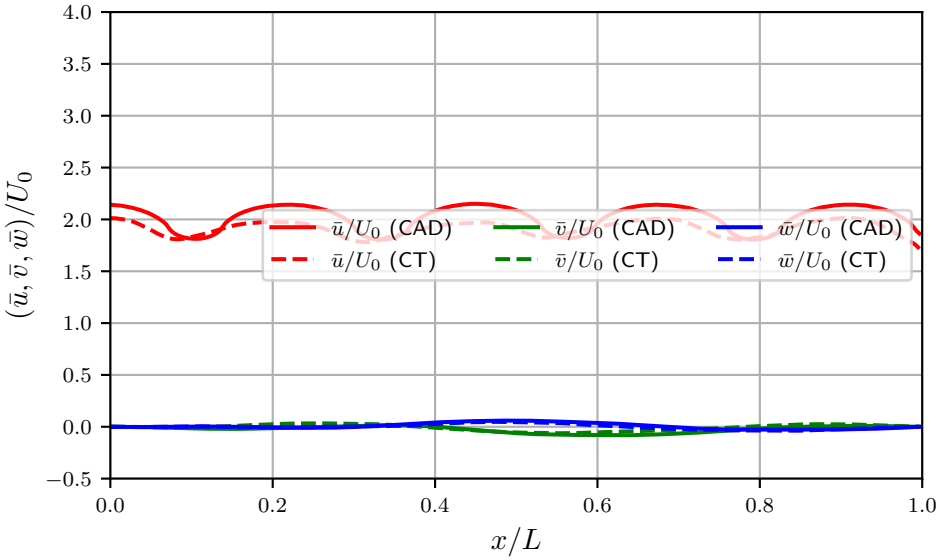

Figure 6: Mean velocity component profiles for Design 2.

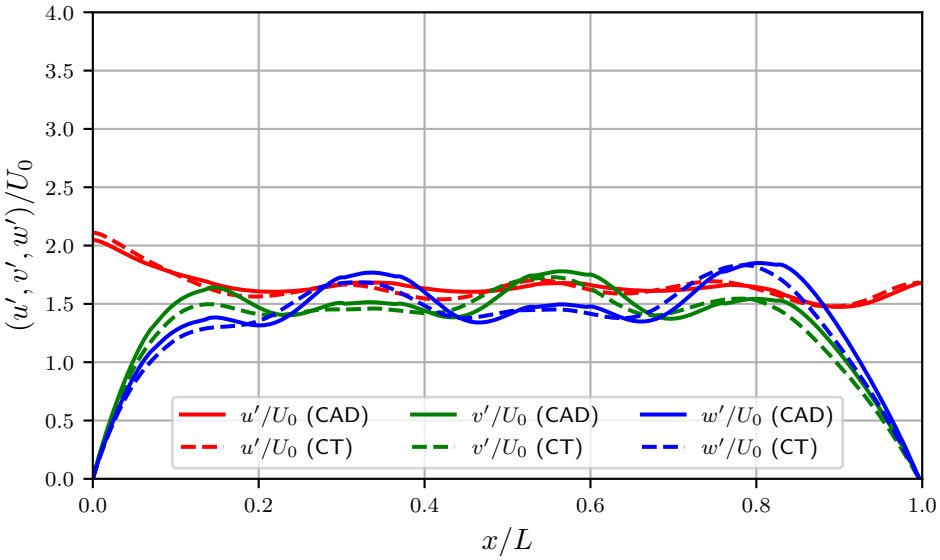

Figure 7: RMS velocity component profiles for Design 2.

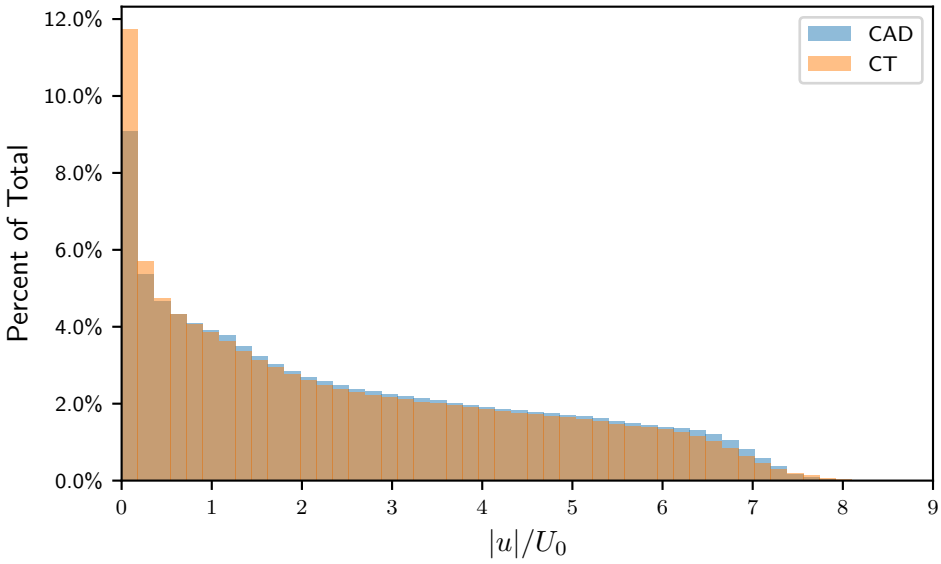

Figure 8: Comparison of velocity magnitude distributions for Design 2.

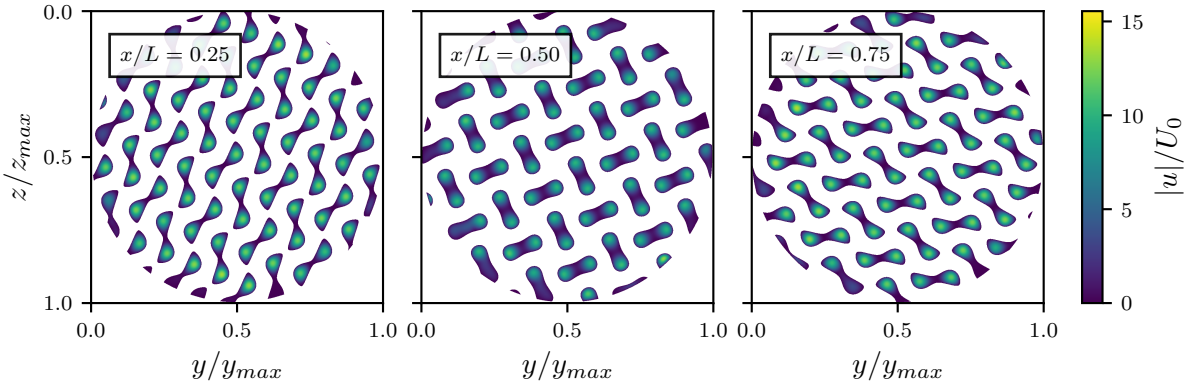

Figure 9: Velocity magnitude profiles at three cross-sectional locations for the CAD data of Design 3.

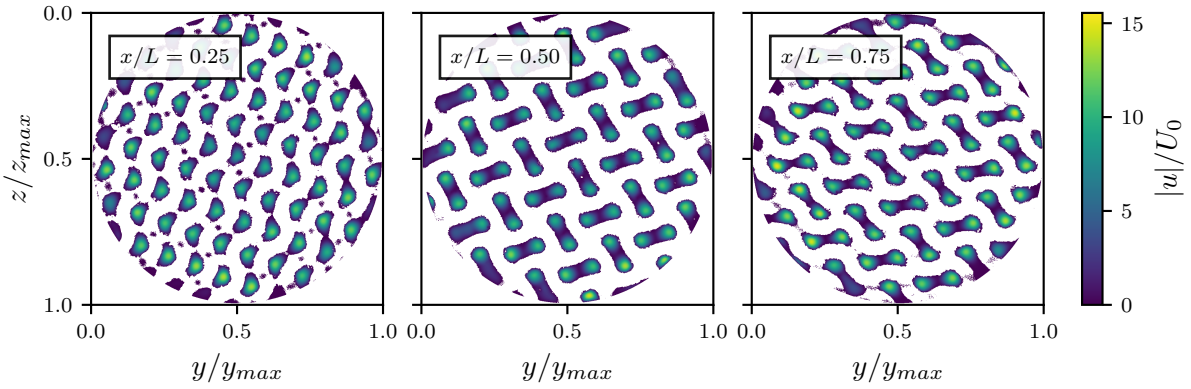

Figure 10: Velocity magnitude profiles at three cross-sectional locations for the CT data of Design 3.

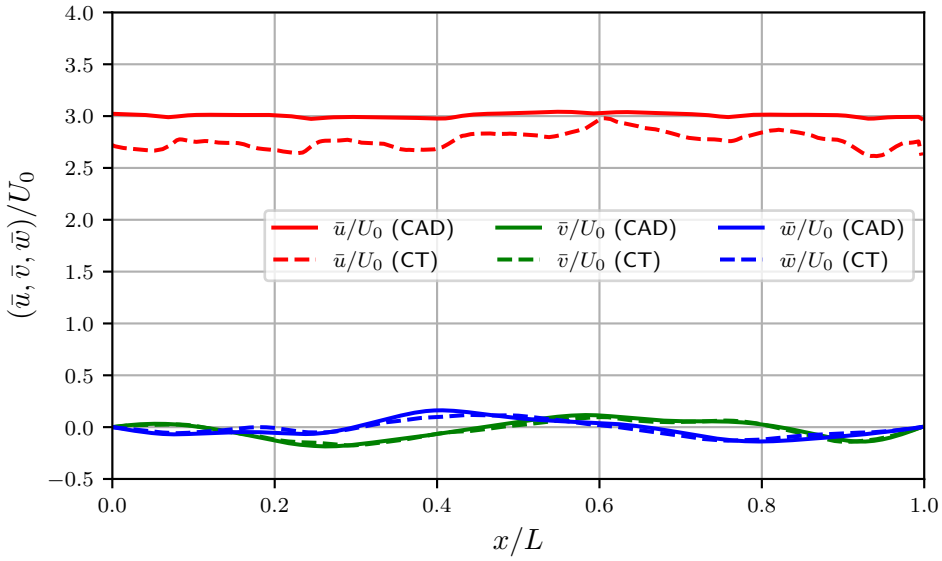

Figure 11: Mean velocity component profiles for Design 3.

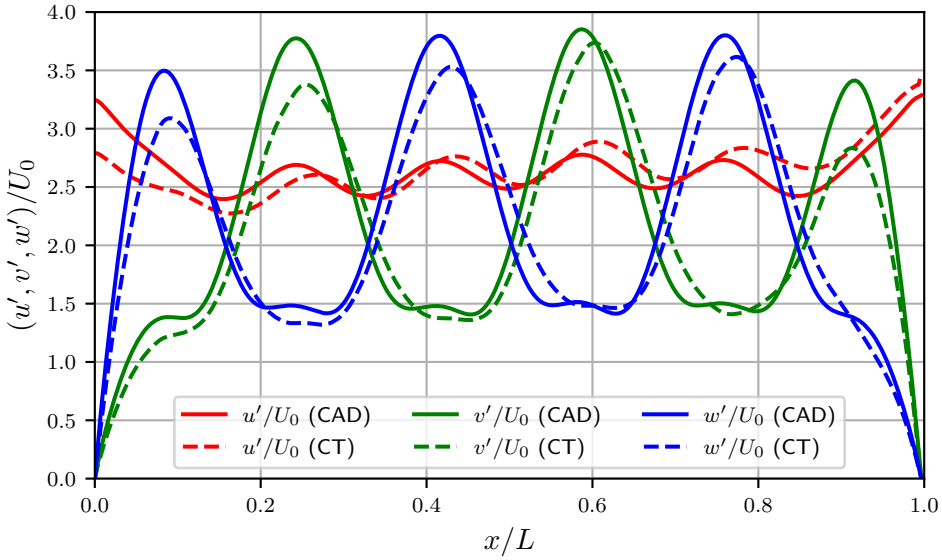

Figure 12: RMS velocity component profiles for Design 3.

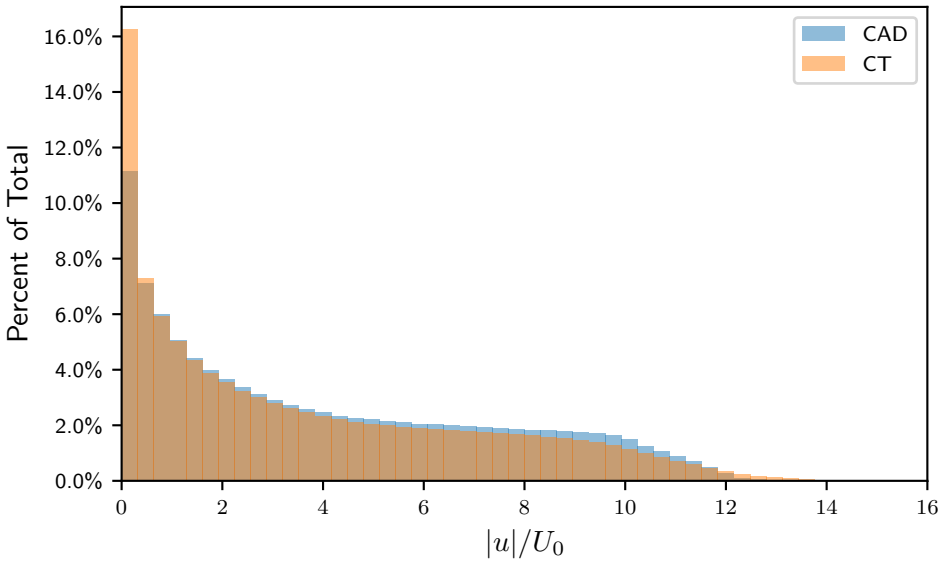

Figure 13: Comparison of velocity magnitude distributions for Design 3.

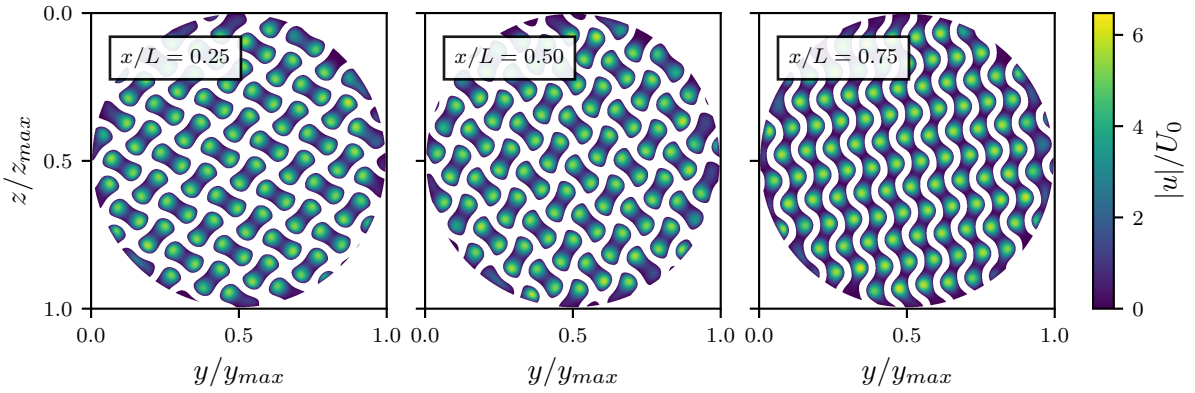

Figure 14: Velocity magnitude profiles at three cross-sectional locations for the CAD data of Design 4.

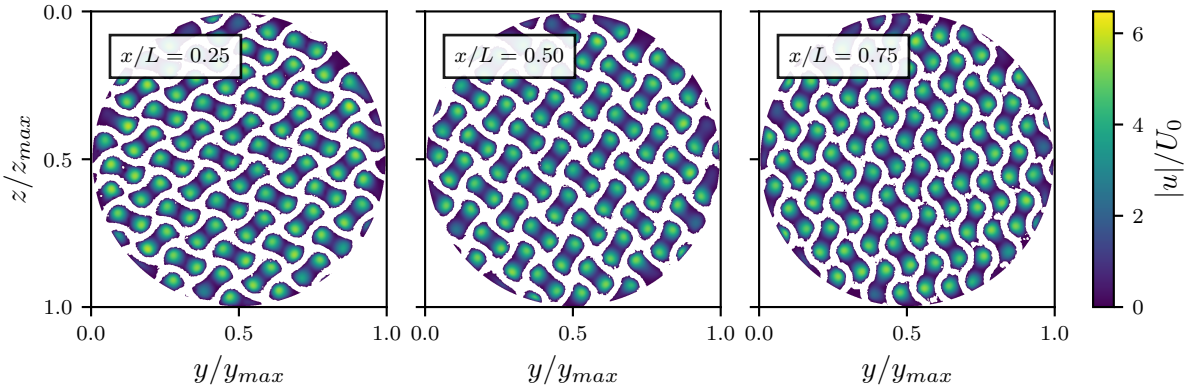

Figure 15: Velocity magnitude profiles at three cross-sectional locations for the CT data of Design 4.

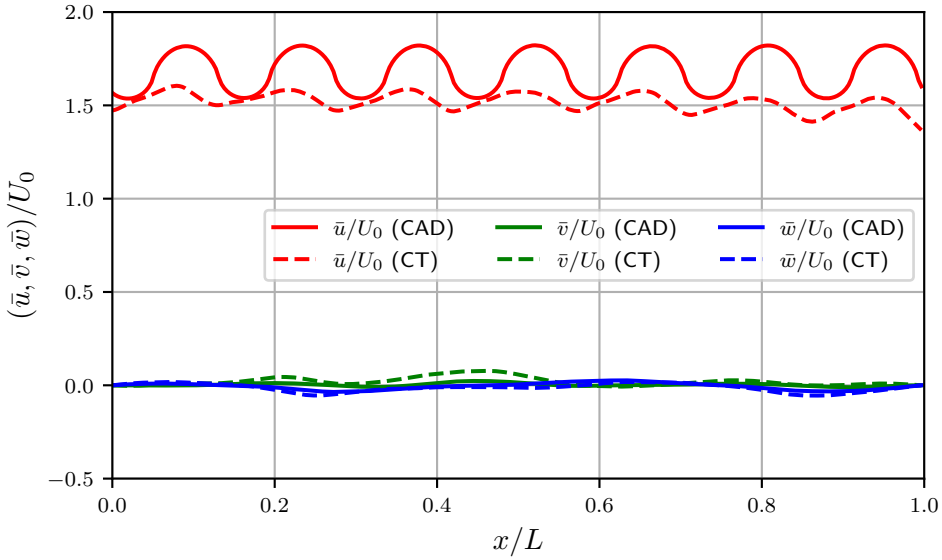

Figure 16: Mean velocity component profiles for Design 4.

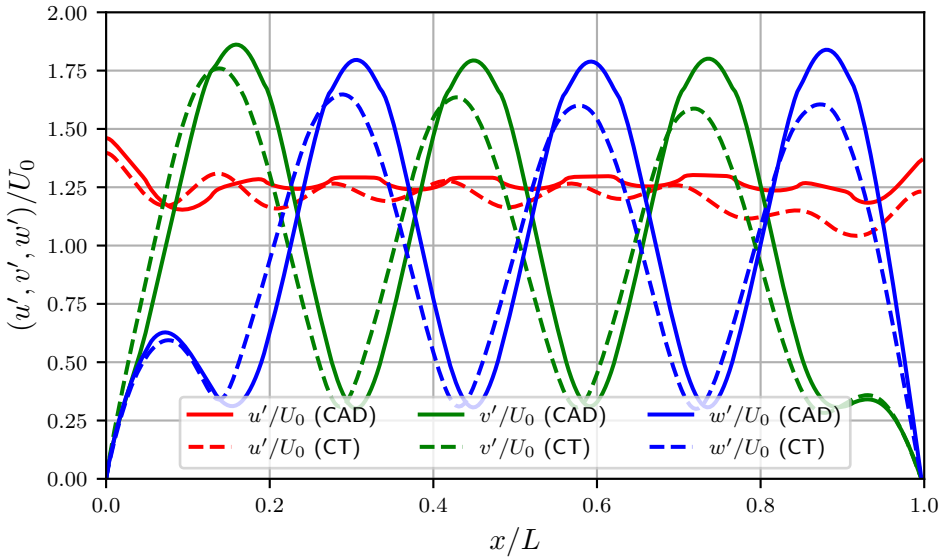

Figure 17: RMS velocity component profiles for Design 4.

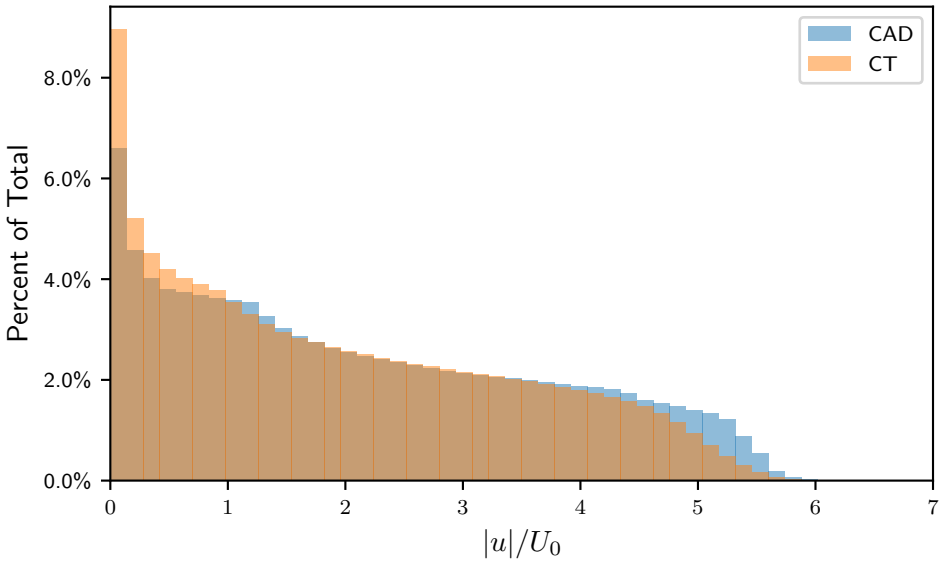

Figure 18: Comparison of velocity magnitude distributions for Design 4.

C Grid Convergence

To demonstrate the independence of the simulation results from the mesh size, a grid convergence study (see Figure C.19) was conducted on the 5 mm unit cell gyroid disk case. Four different meshes were tested for both of the CAD and CT geometries, corresponding to voxel sizes of 120, 60, 30, and 15 µm. The CAD case is well-converged at all mesh sizes, but the same claim cannot be confidently made for the CT case, as asymptotic behaviour is not observed. Since the finest grid resolution assessed was the raw CT resolution, further grid refinement is not meaningfully possible. However, an expected trend occurs in which permeability decreases as the irregular surface morphology becomes better resolved.

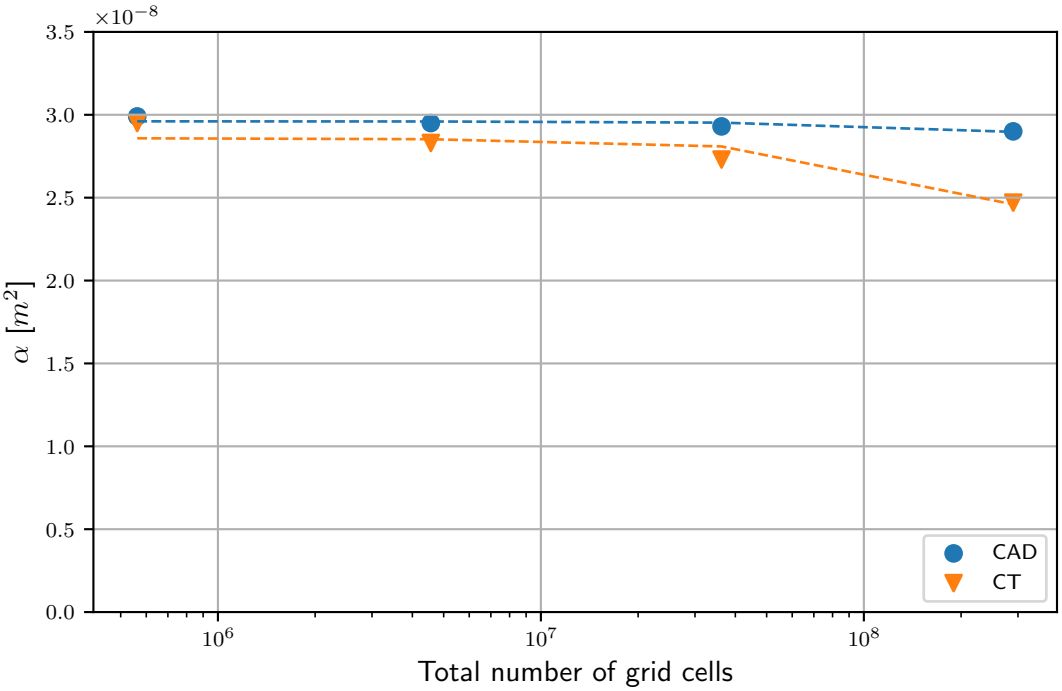

Figure C.19: Grid convergence study for the CAD and CT cases.